Contributions to Mineralogy and Petrology (2024) 179:47
https://doi.org/10.1007/s00410-024-02116-1

ORIGINAL PAPER

# Geochemistry and volatile contents of olivine-hosted melt inclusions from Mt. Etna tholeiitic and alkaline magmatism

P. P. Giacomoni[1] · M. Masotta[1] · G. Delpech[2] · G. Lanzafame[3] · C. Ferlito[3] · J. Villeneuve[4] · M. Coltorti[5]

Received: 3 July 2023 / Accepted: 29 February 2024


## Abstract

The analysis of olivine-hosted melt inclusions (MIs) from the whole sub-alkaline and alkaline magmatic suites of Mt. Etna provides fundamental information about the composition of undifferentiated magmas and their pristine volatile content. Olivine crystals ($Fo_{88-66}$) were selected for Secondary Ion Mass Spectrometry (SIMS) analysis of volatile species ($H_2O$, $CO_2$, F, Cl and S) contained in their host MIs, after preliminary high-pressure/high-temperature re-homogenization, which allowed to reduce the developing of cracks in the host olivine and diffusion-driven outgassing of volatiles from the melt inclusions. This permitted to explore the compositional variability of volatiles of undifferentiated melts and the degassing behavior through the feeding system. The studied MIs show significant major elements compositional heterogeneities (44.57–52.37 wt% $SiO_2$; 3.60–7.51 wt% $Na_2O + K_2O$). Fractionation modelling was performed with Rhyolite-MELTs under variable $fO_2$ regimes ($\Delta$FMQ + 1.5 to + 3), starting from the less evolved MIs compositions and ultimately reproducing most of the observed compositional trends. Mantle melting modelling was used to replicate the observed MIs composition, starting from a spinel-lherzolitic source, accounting for the alkalinity and Fe content of reproduced melts by varying the eutectic contribution of Amph/Phlog and Opx/Cpx respectively. Although most of the studied MIs were degassed in an open-conduit regime, the observed range of volatile concentration in MIs (2.42–6.14 wt% $H_2O$; 308–8474 ppm $CO_2$; 132–697 ppm F; 221–1766 ppm Cl and 16–1992 ppm S) is correlated with a slight decrease in the molar $H_2O/(H_2O + CO_2)$ ratio from early tholeiites to the recent 2015 alkaline products. This observation allows to estimate a minimum 12,250 ppm $CO_2$ and a maximum of 6.14 wt% $H_2O$ in primary melts of the current activity.

**Keywords** Melt inclusions · Magmatic volatiles · Mantle melting · Mt. Etna

## Introduction

Although Mt. Etna is considered a "natural laboratory" for several volcano-related disciplines, many aspects concerning its primitive magma composition and the role of the volatile phases ($H_2O$, $CO_2$, F, Cl, S) in the feeding system are far from being fully comprehended. This uncertainty is further enhanced by the absence of mantle xenoliths and by the extreme scarcity of undifferentiated erupted products, which would provide clues as to the composition of the source(s). Moreover, the eruptive styles documented in historical records span from strictly effusive to strong paroxystic strombolian, without any remarkable difference in major element compositions. Aiming to tackle these issues, recent petrologic studies focused on the geochemistry of olivine-hosted melt inclusions (MIs) as potential archives for primary magma composition and volatile content, especially $H_2O$ and $CO_2$ (Kamenetsky and Clocchiatti 1996; Metrich

Communicated by Othmar Müntener.

✉ P. P. Giacomoni
pierpaolo.giacomoni@unipi.it

[1] Department of Earth Sciences, University of Pisa, Pisa, Italy

[2] Department of Geological Sciences, University of Paris-Saclay, Gif-Sur-Yvette, France

[3] Department of Biological, Environmental and Geological Sciences, University of Catania, Catania, Italy

[4] Centre de Recherches Pétrographiques et Géochimiques, CNRS Nancy, Vandœuvre-Lès-Nancy, France

[5] Department of Physics and Earth Sciences, University of Ferrara, Ferrara, Italy

Published online: 22 April 2024

et al. 2004; Gennaro et al. 2019). These micrometric droplets of magma are trapped during crystal growth thus potentially sampling and preserving the composition of the magma, including its volatile content at the time of entrapment.

Among the available basic products, there is a general agreement in considering the lavas from Mt. Maletto (~7 Ka; Kamenetsky and Clocchiatti 1996; Schiano et al. 2001), Mt. Spagnolo (< 14,000 B.P.; Branca et al. 2011) and FS Tephra (3939 ± 60 B.P., Coltelli et al. 2005) eruptions as the least differentiated products of the alkaline series although they underwent a maximum of 10% of Ol fractionation en-route to the surface (Giacomoni et al. 2014). The volatile contents in olivine-hosted MIs are extremely variable, with a maximum of 6 wt% $H_2O$ and 6000 ppm of $CO_2$ in FS, and up to 4300 ppm S in Mt. Spagnolo, yielding to a depth range of 4–19 km (below crater level), as estimated by means of $H_2O$ and $CO_2$ solubility models (Metrich and Clocchiatti 1989; Metrich et al. 2004; Gennaro et al. 2019). These data indicate that the feeding system of Mt. Etna is relatively enriched in volatiles and, coupled with gaseous emissions from crateric fumaroles, define Mt. Etna as one of the strongest emitters of magma derived volatiles on Earth (Allard et al. 1991; Aiuppa et al. 2008; Burton and Sawyer 2013).

In this study, we contribute to the characterization of primary magma composition and on the origin of volatiles ($H_2O$, $CO_2$, S, F, Cl) in Mt. Etna primary magmas through the geochemical characterization of olivine-hosted MIs representative of the four main phases of magmatism: early tholeiites, Ellittico (Ancient Mongibello), Pre-historic Mongibello and recent 2015 eruptions.

The most efficient approach to obtain a homogenous glass from re-crystallized MIs is based on re-heating the inclusion using a heating stage or a vertical furnace up to a complete homogenization of post entrapment crystallization and vapor bubbles by observing the MIs under an optical microscope. The major limitations of this technique are that, during heating at 1 atm, the increase in the internal pressure of the MI can cause the brittle or plastic deformation of the host mineral (Ferrero and Angel 2018; Schiavi et al. 2016; Wallace et al. 2021) and the lack of total homogenization of $CO_2$-rich vapour bubbles (Buso et al. 2022). To overcome these problems, we performed MIs re-homogenization at high pressure and temperature (HP-HT), using a piston cylinder apparatus. High pressure homogenization potentially reduces the decrepitation of the MIs and allows for a complete dissolution of all the volatile species that are present in the bubbles back into the MIs melt. (Stefano et al. 2011; Hudgins et al. 2015).

## Geological and volcanological background

The volcanological evolution of the etnean area has been described and defined in distinct supersynthems by Branca et al (2011) and here briefly summarized. Magmatism in Mt. Etna area started ~ 550 Ka with the emission of subaqueous lava flows and hyaloclastic breccias with tholeiitic affinity. The products of this discontinuous activity, defined as Basal Tholeiitic Supersynthem, currently outcrop along the eastern coast of Sicily. From ~ 220 to ~ 110 Ka (Timpe Supersynthem) magmatism gradually shifted from subaqueous to subaerial and concomitantly from tholeiitic to Na-alkaline compositions. The transition from fissural activity to several dispersed central conduit edifices marks the onset of the Ancient Alkaline Volcanism (AAV) started at ~ 110–65 Ka (Tanguy et al. 1997). Most of the products of this activity outcrop in the southern flank of the Valle del Bove, constituting the Valle del Bove Supersynthem.

The eruptive activity gradually shifted toward a central conduit feeding system, this period has been defined as Stratovolcano Supersynthem (57 ka-now) and can be divided in two distinct stages: Ellittico (57–15 ka) and Mongibello (< 15 ka-now). The Ellittico activity was characterized by the emission of alkaline products with Na-affinity, ranging from hawaiitic to trachytic in composition. A Plinian eruption and subsequent caldera collapse marked the end of this stage as testified by the Biancavilla-Montalto ignimbrites. Subsequent Recent Mongibello products filled the caldera depression with hawaiitic lava flows and strombolian deposits. From 2138 BP to present days, eruptions occurred at the summit craters and along three main lateral feeding systems namely W, S and NE Rifts.

A slight increase in the $K_2O$ content of magmas, whose affinity moved from sodic to potassic (Tanguy et al. 1997) has been documented starting from the 1971 eruptive event. However, a bi-modal sodic + potassic affinity of the erupted products was already documented for older Ellittico (Ferlito and Lanzafame 2010), in post-1972 products and contemporaneously emitted during the 2002/2003 eruption (Ferlito et al. 2009; Giacomoni et al. 2012).

In this context, recent geophysical, geochemical and petrological studies (Andronico et al. 2008; Ferlito et al. 2009; Giacomoni et al. 2021) of eruptive events occurring from 2001 to 2014 agree that the geometry of feeding conduits and changes in the physical–chemical (P-T-$fO_2$-$XH_2O$-$XCO_2$) parameters should be considered as the main factors governing the eruptive styles rather than magma composition. The intense paroxystic eruption which occurred between 3 to 8th December 2015 demonstrated that magma residing at different levels inside the

vertical central feeding system erupts as consequence of flushing of the volatiles exsolved by the incoming basic magma (Giacomoni et al. 2021).

## Sampling criteria, lava and melt inclusions petrography

### Sampling

Rock samples were collected from four localities, representative of the most relevant discontinuities during volcanological evolution in the etnean area (Fig. S1). Samples from the tholeiitic phase (ET4) were collected from the early subaerial lava flows outcropping at the Rocca of Aci Castello while products from the Ellittico (ET51) activity were sampled at the northern wall of Valle Del Bove at the Serracolle locality. Pre-historic recent Mongibello studied lavas (ET45) were collected from Mt. Nero delle Concazze scoria cone sited on the northern flank in the nearby of Piano Provenzana. Finally, 2015 samples were collected during the paroxysmal activity that occurred between December 3rd to December 8th, 2015 (Giacomoni et al. 2021). Two samples are pyroclastic bombs collected nearby the Central Craters and North East Crater, one sample was collected from a lava flow outpoured from the eastern flank of New South East Crater.

Seven hand-size rock samples have been selected based on the amount of olivine phenocrysts, potentially hosting valuable MIs (Fig.S2). Eighty-eight (88) olivine-grains from 500 mm to 1.5 mm in size were separated from lava samples, hand-picked and individually observed under microscope to recognize the MIs (Fig. 1a-b). Olivine crystals containing MIs (> 50 µm in diameter) were mounted on epoxy blocks for chemical analysis, whereas fractured olivine grains were discarded.

### Petrography and composition of host olivine crystals

Tholeiitic samples are low porphyritic (Porphyritic Index; P.I. ~ 12%) characterized by a phenocryst assemblage of olivine (Ol, 12%) + orthopyroxene (Opx, 18%) + clinopyroxene (Cpx, 20%) + plagioclase (Plg, 34%) and magnetite (Mt, 16%) embedded in glassy to microcrystalline matrix. The volume percentage of vesicles varies from 10 to 18%. Lavas from the Ellittico phase show a higher content of phenocrysts (P.I. ~ 24%) in the following relative proportions: Ol (8%) + Cpx (34%) + Plg (48%) and Mt (10%). Vesicle volume percentage varies from 8 to 14%. The microcrystalline matrix is mainly composed of Plg and micrometric acicular apatite (Ap), frequently shows a fluidal mingling texture. Samples from the Recent Mongibello phase are high porphyritic (Porphyritic Index; P.I. ~ 22%), made of Ol (12%) + Cpx (34%) + Plg (40%) and Mt (14%) embedded in an almost glassy matrix. Vesicle volume percentage is ~ 12%. Lavas from the 2015 activity are low to mid porphyritic (Porphyritic Index; P.I. ~ 8–16%) and show a phenocryst assemblage made of Ol (18%) + Cpx (44%) + Plg (30%) and Mt (8%) embedded in a microcrystalline matrix. The volume percentage of vesicles varies from 14 to 20%.

The Fo content of host olivine varies significantly: from 83 to 85 in tholeiitic samples, from 67 to 77 in the Ellittico, from 70 to 78 in Recent Mongibello and from 66 to 88 in the 2015 eruption (Table S1).

Olivine phenocrysts selected for homogenization experiments were euhedral without any trace of weathering or radial cracks (Fig. 1a, b). Each crystal hosted up to 5 brownish MIs, varying in shape from almost spherical to slightly elongated, and from < 10 µm to 300 µm in diameter.

### Petrography of melt inclusions: before and after homogenization

Host olivine crystals were observed under a binocular microscope with the aim to identify those containing feasible melt inclusions before the HP-HT homogenization. Olivine grains were deepened in ethyl alcohol during observation, this foresight allow to better see through the crystals and to identify the inclusions entrapped at different depth.

Before homogenization, most of MIs were crystallized (~ 60%) and exhibited a daughter crystal assemblage made of Cpx (40–70%), Ol (5–25%), Fe-Ti oxides (5–10%) and Cr-Spinel (< 5%). Daughter crystals were mostly anhedral or acicular and ranged in size from < 5 µm up to 40 µm (along the major axis). Shrinkage bubbles were present in 30% of studied MIs. The estimated volume of the fluid phase ranges from 5 to 14. MIs from the Tholeiitic Phase show more frequently an exsolved volatile phase, while MIs from the recent 2015 paroxystic event are almost totally glassy (Fig. 1c, d, e).

After HP-HT homogenization experiments, most of the MIs (ca. 90%) resulted glassy, whereas a small amount (10%) preserved micrometric Cpx and/or Ti-magnetite with an anhedral shape (spinifex or dendritic). Among the non-homogenized grains, about half preserved an exsolved fluid phase. These non-homogenized MIs were discarded. Compositional SEM–EDS maps show that Fe–Mg re-equilibration between MI and host olivine was limited to a narrow (< 10 µm thick) rim inside the olivine (Fig. 2a-b). This observation leads to considering applying a post-entrapment correction (PEC) to the major and minor element composition, which is described in detail in section "Post-entrapment modifications and correction".

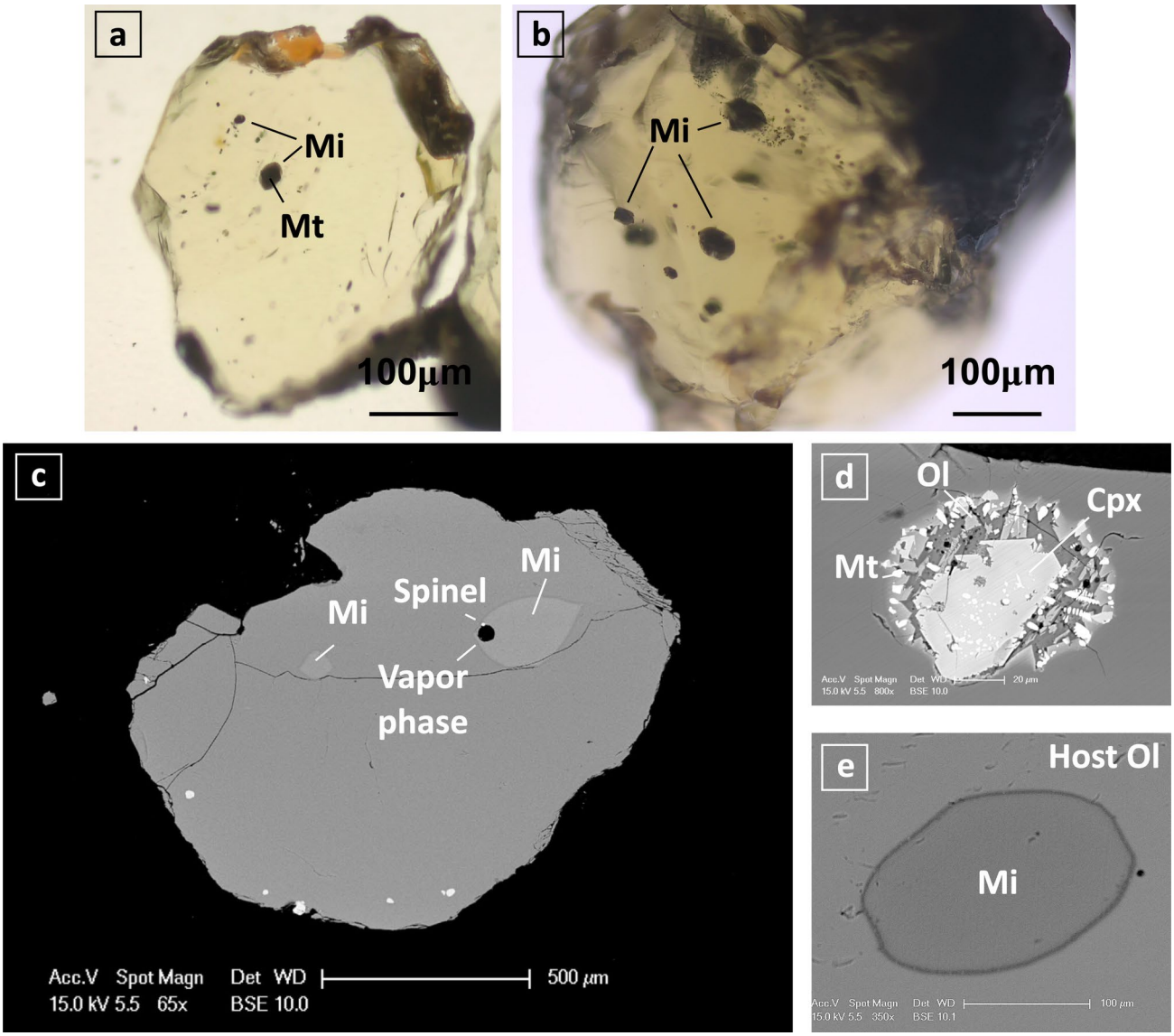


**Fig. 1** Microphotographs of studied a MIs hosting olivine crystal before and after HP-HT homogenization experiments. In panels **a** and **b**; transmitted light microphotographs of olivine grains containing several MIs before re-homogenization experiments. **c** Backscattered SEM images of olivine hosting melt-inclusion after the homogenization experiment, showing a homogeneous inclusion close to a MI still preserving an exsolved fluid phase and a spinel crystal. **d** re-crystallized inclusion containing daughter Cpx, Ol and Mt; **e** MI after HP-HT re-homogenization

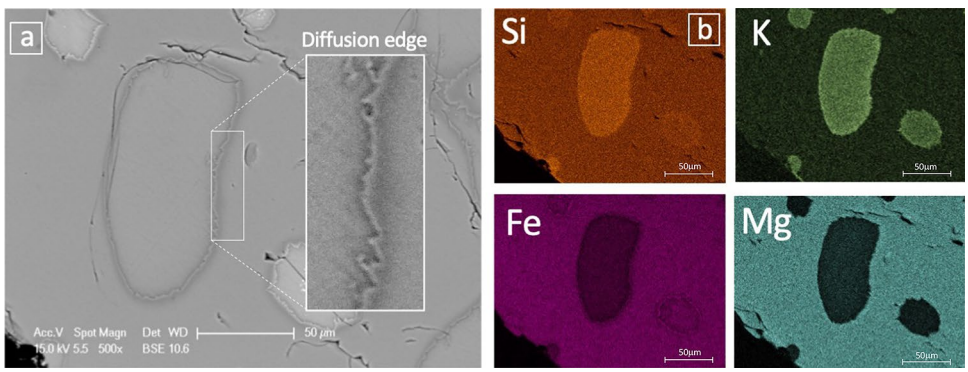


**Fig. 2** Backscattered SEM image of a melt-inclusion post HP-HT homogenization showing a diffusion edge at the contact with the host-olivine and electron compositional maps of Si, K, Fe and Mg (**b**)

### MIs homogenization experiments

MIs homogenization experiments were performed at the HP-HT Laboratory of the University of Rochester (USA), using an end-load piston cylinder apparatus. Picked crystals were dried in a ceramic vessel at 110 °C for 2 h with the aim to eliminate hygroscopic water. Olivine grains (10–15) were inserted in a graphite capsule and packed with graphite powder. A standard ¾" assembly composed of an NaCl cell, borosilicate glass, graphite and crushable MgO was used for the experiments (Fig. S3 and Watson et al. 2002). Temperature was maintained constant at the setpoint (within 5 °C) and monitored using a type D ($W_{97}Re_3/W_{75}Re_{25}$) thermocouple for the entire run duration. The experimental run-up involved cold pressurization to a value exceeding the desired run pressure (6 Kbar) by 10–20%, allowing for "settling" (relaxation) of the assembly upon heating and final adjustments to the desired pressure value. Temperature was increased to 1300 °C at a rate of about 100 °C/min and held for 20 min before isobaric quench at a rate about 100 °C/s. Olivine grains were mounted in epoxy resin and polished until melt inclusions were exposed. A microscopic observation of the prepared mounts allowed to discard not fully homogenised inclusions (~ 10% with daughter crystals and/or gaseous phase) or those showing radial crack.

Under the experimental conditions (1300 °C and 6 Kbar), according to the diffusion modelling by Zhang and Stolper (1991) and Chen and Zhang (2008), melt homogenization occurs rapidly enough to preserve the bulk chemistry of the MI, minimizing the volatile diffusion in or out of the olivine crystal. The short homogenization time of 20 min also prevents carbon contamination from the surrounding graphite, considering the low solubility and diffusivity of C in olivine, 0.1–1 ppm and $< 10^{-12}$ $cm^2/s$ respectively (Tingle et al. 1988; Keppler et al. 2003; Shcheka et al. 2006).

### Analytical methods

Bulk rock geochemical analyses of were performed at the Department of Physics and Earth Sciences, University of Ferrara (Italy). Major and some trace elements (Ba, Cr, Sc, V, Ni, Cu) concentrations were determined by X-ray fluorescence (Thermo ARL Advant XP). The matrix effects on measured intensities were corrected using the method of Lachance and Traill (1966); loss on ignition (L.O.I.) was determined by gravimetric method, assuming $Fe_2O_3$ as 15% FeO (Roeder and Emslie 1970). The remaining trace elements (Zr, Rb, Sr, Hf, Nb, Ta, Th, U, Y) and REE concentrations were measured by inductively coupled plasma mass spectrometry (ICP-MS) on a VG Elemental Plasma Quad 2Plus instrument. The data reproducibility ranges between 0.7% and 7.2% with an accuracy of 10% and a detection limit of 10 ppb for Th, U and REE.

Polished mounts containing the olivine grains were then carbon coated and major and minor elements analyses of individual MIs and host olivines were measured by electron microprobe (EMPA, Cameca SX100), at the Department of Lithospheric Science, University of Wien (Austria). Measurements of MIs were made with an accelerating voltage of 15 kV, a beam current of 10 nA, and a 5 µm defocused beam, while host olivines were analysed with 15 kV acceleration voltage, 20 nA current and a 3 µm wide focused beam. A 20 s counting time was chosen for major elements, while background counting times were half of the peak counting time. Detection limits were typically in the range of 0.02–0.06 wt%.

A total of 34 homogenized and cracks-free inclusions were analysed for their concentrations in of $H_2O$, $CO_2$, F, Cl and S with a CAMECA 1280 IMS HR2 ion microprobe (SIMS) at Centre de Recherches Pétrographiques et Géochimiques (CRPG) of Nancy (France). Selected olivine grains were re-polished after EPMA to remove the carbon coating, removed from the epoxy mount and then pressed into an aluminium disk filled with indium, together with standard reference glasses. The indium mount was then re-polished, washed and stored under vacuum prior to being gold coated and outgassed in the ion microprobe samples storage. A liquid nitrogen trap was used in order to keep the vacuum below $3 \times 10^{-9}$ bar in the analysis chamber. MIs were sputtered with an 8 mm wide and 0.5 nA $^{133}Cs+$ primary ion beam accelerated at 20 kV. To eliminate any surface contamination, each spot was sputtered with a rastered beam ($10 \times 10$ mm) for 240 s prior to analysis.

Secondary ions of $^{12}C^-$, $^{16}OH^-$, $^{19}F^-$, $^{30}Si^-$, $^{32}S^-$ and $^{35}Cl^-$ counted in monocollection mode either on an electron multiplier or a Faraday cup during 8 s, 6 s, 6 s, 4 s, 4 s, 4 s per cycle respectively and for 10 cycles. A set of nine natural and synthetic standards of volatile and halogens-bearing basaltic glasses was used for the calibration: Macusani enriched glasses (M34, M35, M40, M43, M48 from Shishkina et al. 2010); halogens-rich glasses (47,963, 60,701, 25,603 from Bindeman et al. 2012) and KL2G (Jochum et al. 2006). Typical uncertainties on $H_2O$, $CO_2$, F, Cl and S contents are ± 1% relative.

## Results

### Whole rock and MIs composition

Whole-rock major element compositions of Mt. Etna lavas are plotted in a Total Alkali Silica diagram (Fig. 3) together with a literature dataset and reported in Table 1. The composition of lavas is generally well consistent with those reported by previous studies (Tanguy et al. 1997; Spilliaert et al. 2006a; Gennaro et al. 2019), falling in the

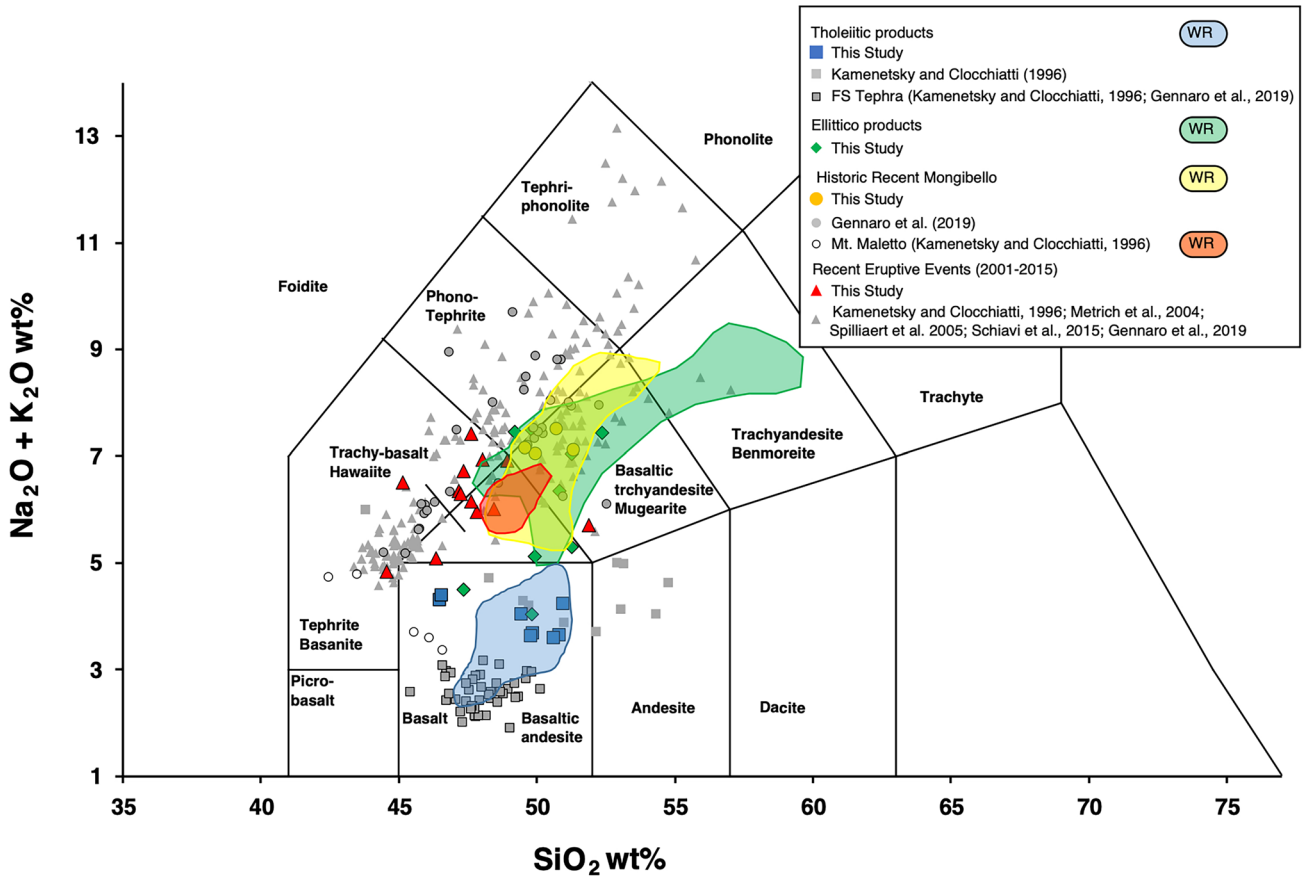


**Fig. 3** Volcanic rock total alkali-silica classification diagram (Le Bas et al. 1986) of Mt. Etna whole rock and MIs compositions. Studied MIs are colored plotted: blue squares (Tholeiitic Phase); green diamonds (Ellittico Phase); orange circles (Recent Mongibello); red triangles (2015 eruptive event). Bibliographic data of Mt. Etna MIs are plotted in grey,whole rock (WR) are represented by colored fields

fields of subalkaline and alkaline products. Sub alkaline tholeiitic products vary from 48.09 to 48.43 wt% $SiO_2$ and from 2.46 to 2.71 in total alkali content ($Na_2O + K_2O$ wt%). Alkaline samples (Ellittico, Recent Mongibello and 2015 eruption) fall in the fields of hawaiites and trachybasalts (47.99–49.14wt% $SiO_2$; 5.75–6.24 wt% $Na_2O + K_2O$; Table 1).

The major element concentration of studied MIs is summarized in Table 2 and compared with their host rock composition together with whole-rock and MIs bibliographic dataset (Figs. 3 and 4); both originals (without PEC correction) and after post-entrapment correction (see section "Post-entrapment modifications and correction") are reported, however, only the latter are plotted in the figures for best comparison with the literature dataset. Compared to whole-rock compositions, MIs are generally less evolved, covering the range of compositions reported in previous studies (Kamenetsky and Clocchiatti 1996; Kamenetsky et al. 2007; Del Carlo and Pompilio 2004; Spilliaert et al. 2006a and b; Schiavi et al. 2015; Gennaro et al. 2019). MIs from subalkaline samples mostly plot in the fields of basalts while inclusions from the Ellittico and Recent Mongibello can be classified as hawaiites (Fig. 3). MIs from the 2015 eruption cover a wider range of magma composition, ranging from trachybasalts to basanites (Fig. 3), and compare well with the compositions of Mt. Maletto and Mt. Spagnolo (Gennaro et al. 2019). The majority of studied MIs are basic, with a Mg# (calculated as $[Mg/(Mg + Fe^{2+}{}_{Tot})*100]$), ranging from 38.6 to 68.5. The $FeO_{Tot}$ versus $SiO_2$ diagram (Fig. 4a) highlights the high content in $FeO_T$ of most of the studied samples (ranging from 8.5 to 13.7 wt%). Similar high $FeO_T$ values are reported in the literature (Schiavi et al. 2015; Gennaro et al. 2019), the studied alkaline MIs depict a trend of decreasing in $FeO_T$ with decreasing $SiO_2$. From these high $FeO_T$ contents, some MIs appear to be aligned with the literature trend of decreasing $FeO_T$ together with MgO content, which is also typical of Etnean lavas.

The studied MIs present marked variations in $K_2O$ concentrations vs $SiO_2$ and MgO (Fig. 4b) that are comparable to the literature data and confirms the overall enrichment in $K_2O$ with time (Tanguy et al. 1997; Schiavi et al. 2015; Gennaro et al. 2019).

**Table 1** Whole rock compositions of studied lavas. Mg# = MgO/(MgO + FeOt) mol%

| Volcanic Phase | Tholeiite | Tholeiite | Ellittico | Rec. Mongibello | 2015 | 2015 | 2015 |
|---|---|---|---|---|---|---|---|
| Sample | ET4a | ET6 | ET51 | ET45 | NECr | CCr | SE-Xr |
| $SiO_2$ (wt%) | 48.09 | 48.43 | 48.89 | 47.99 | 48.68 | 49.14 | 48.52 |
| $TiO_2$ (wt%) | 1.49 | 1.39 | 1.58 | 1.76 | 1.78 | 1.72 | 1.65 |
| $Al_2O_3$ (wt%) | 13.65 | 13.57 | 17.80 | 17.30 | 17.14 | 17.32 | 17.85 |
| FeO (wt%) | 9.44 | 9.38 | 9.33 | 9.38 | 9.37 | 8.83 | 9.07 |
| $Fe_2O_3$ (wt%) | 1.42 | 1.41 | 1.40 | 1.41 | 1.40 | 1.32 | 1.36 |
| MgO (wt%) | 8.14 | 8.64 | 4.20 | 4.77 | 5.05 | 5.06 | 4.44 |
| MnO (wt%) | 0.15 | 0.10 | 0.16 | 0.19 | 0.19 | 0.18 | 0.17 |
| CaO (wt%) | 15.00 | 14.27 | 9.85 | 10.90 | 10.27 | 10.17 | 10.90 |
| $Na_2O$ (wt%) | 2.18 | 2.31 | 4.42 | 3.82 | 3.68 | 3.75 | 3.94 |
| $K_2O$ (wt%) | 0.28 | 0.40 | 1.82 | 2.06 | 2.07 | 2.05 | 2.05 |
| $P_2O_5$ (wt%) | 0.17 | 0.10 | 0.54 | 0.43 | 0.36 | 0.46 | 0.05 |
| Totale | 100 | 100 | 100 | 100 | 100 | 100 | 100 |
| Mg# | 73.84 | 72.98 | 44.41 | 47.45 | 3.51 | 3.52 | 3.25 |
| Alkali Sum | 2.46 | 2.71 | 6.24 | 5.88 | 5.75 | 5.80 | 5.99 |
| Sc (ppm) | 25.3 | 18.1 | 14.7 | 22.9 | 27.5 | 22.4 | 25.5 |
| Ni (ppm) | 249 | 159.5 | 19.6 | 14.1 | 10.8 | 14.8 | 9.9 |
| Co (ppm) | 67 | 53.8 | 36.5 | 40.9 | 37.4 | 38.5 | 26.4 |
| Cr (ppm) | 527.2 | 271.5 | 48.3 | 38.7 | 27.1 | 34.4 | 38.8 |
| Cu (ppm) | 72.8 | 85.5 | 78.5 | 137.7 | N.D | N.D | N.D |
| Zn (ppm) | 84.3 | 85.6 | 73 | 82 | N.D | N.D | N.D |
| Ga (ppm) | 13.2 | 15.8 | 19.7 | 17.9 | 21.8 | 20.5 | 20.3 |
| Rb (ppm) | 6.9 | 7.0 | 44.7 | 51.4 | 47.7 | 46.6 | 46.5 |
| Ba (ppm) | 129.6 | 199.1 | 744.0 | 658.5 | 650.9 | 644.2 | 644.9 |
| Th (ppm) | 2.0 | 2.9 | 14.6 | 8.6 | 13.5 | 10.2 | 12.4 |
| U (ppm) | 1.0 | 1.0 | 4.0 | 3.1 | N.D | N.D | N.D |
| Nb (ppm) | 13.7 | 23.0 | 59.0 | 47.3 | 49.2 | 49.5 | 45.8 |
| Ta (ppm) | 0.7 | 1.0 | 2.5 | 2.1 | N.D | N.D | N.D |
| La (ppm) | 16.3 | 25.0 | 74.1 | 65.0 | 60.5 | 65.3 | 75.7 |
| Ce (ppm) | 33.6 | 49.5 | 128.5 | 119.1 | 113 | 111.2 | 122.6 |
| Pr (ppm) | 4.1 | 5.6 | 14.4 | 12.9 | N.D | N.D | N.D |
| Sr (ppm) | 328.4 | 500.3 | 1048.1 | 1135.1 | 1243 | 1183 | 1212 |
| Nd (ppm) | 18.0 | 23.5 | 54.0 | 51.8 | 44.4 | 47.3 | 24.3 |
| Sm (ppm) | 4.2 | 5.1 | 9.3 | 9.5 | N.D | N.D | N.D |
| Hf (ppm) | N.D | N.D | N.D | N.D | 5.9 | 4.9 | 6.1 |
| Zr (ppm) | 99.0 | 125.6 | 224.7 | 225.2 | 129.8 | 152.1 | 58.5 |
| Eu (ppm) | 1.4 | 1.8 | 2.7 | 2.8 | N.D | N.D | N.D |
| Gd (ppm) | 4.2 | 5.1 | 8.0 | 8.3 | N.D | N.D | N.D |
| Tb (ppm) | 0.7 | 0.8 | 1.2 | 1.2 | N.D | N.D | N.D |
| Dy (ppm) | 3.7 | 3.9 | 5.0 | 5.5 | N.D | N.D | N.D |
| Y (ppm) | 27.0 | 27.2 | 35.5 | 35.5 | 30.9 | 30.9 | 31.8 |
| Ho (ppm) | 0.7 | 0.7 | 1.0 | 1.0 | N.D | N.D | N.D |
| Er (ppm) | 1.9 | 1.9 | 2.5 | 2.7 | N.D | N.D | N.D |
| Tm (ppm) | 0.3 | 0.3 | 0.4 | 0.4 | N.D | N.D | N.D |
| Yb (ppm) | 1.7 | 1.5 | 2.2 | 2.3 | N.D | N.D | N.D |
| Lu (ppm) | 0.3 | 0.2 | 0.3 | 0.3 | N.D | N.D | N.D |

In the CaO vs $SiO_2$ and $CaO/Al_2O_3$ vs MgO diagrams (Fig. 4c-d), studied MIs plot on a wide range of CaO contents (9.6–14.3 wt%), significantly more calcic than erupted lavas, but comparable to published data from Mt. Maletto, FS-Tephra and recent eruptive events. Both CaO and $CaO/Al_2O_3$ decrease with decreasing MgO, however, whole rock

**Table 2** Original and PEC (Post Entrapment Crystallization) corrected composition of studied MIs. Mg#=MgO/(MgO+FeOt) mol

| Period | Tholeiite | Tholeiite | Tholeiite | Tholeiite | Tholeiite | Tholeiite | Tholeiite | Tholeiite | Ellittico | Ellittico | Ellittico | Ellittico | Ellittico | Ellittico | Ellittico | Ellittico |
|---|---|---|---|---|---|---|---|---|---|---|---|---|---|---|---|---|
| Sample | ET4 | ET4 | ET4 | ET4 | ET4 | ET4 | ET4 | ET4 | ET 51 | ET 51 | ET 51 | ET 51 | ET 51 | ET 51 | ET 51 | ET 51 |
| Host crystal | Ol 1 | Ol 1 | Ol 1 | Ol 1 | Ol 2 | Ol 2 | Ol 4 | Ol 4 | Ol 5 | Ol 5 | Ol 6 | Ol 6 | Ol 6 | Ol 6 | Ol 7 | Ol 8 |
| DataSet/Point | 1/1 | 1/2 | 5/1 | 5/2 | 7/1 | 8/1 | 15/1 | 17/1 | 18/1 | 18/2 | 21/1 | 24/1 | 26/1 | 28/1 | 31/1 | 34/1 |
| $SiO_2$ (wt%) | 48.4 | 48.2 | 47.3 | 47.3 | 43.4 | 43.3 | 47.0 | 46.6 | 47.9 | 48.4 | 43.9 | 47.3 | 46.6 | 46.2 | 47.7 | 46.4 |
| $Al_2O_3$ (wt%) | 11.8 | 11.9 | 11.7 | 11.7 | 11.5 | 11.4 | 13.1 | 11.0 | 12.7 | 12.2 | 11.0 | 11.4 | 10.3 | 10.9 | 11.1 | 11.8 |
| $TiO_2$ (wt%) | 1.6 | 1.6 | 1.5 | 1.5 | 1.6 | 1.6 | 1.6 | 1.6 | 2.0 | 1.8 | 1.6 | 2.1 | 1.8 | 1.7 | 1.4 | 1.9 |
| FeOT (wt%) | 9.7 | 9.7 | 9.5 | 9.6 | 10.5 | 10.5 | 9.8 | 9.9 | 10.4 | 10.1 | 12.7 | 12.3 | 12.4 | 12.6 | 11.2 | 12.6 |
| MgO (wt%) | 11.9 | 11.7 | 12.8 | 12.7 | 11.6 | 12.2 | 12.5 | 12.3 | 10.7 | 10.5 | 10.3 | 12.3 | 10.0 | 10.5 | 12.6 | 12.2 |
| CaO (wt%) | 11.1 | 11.2 | 11.5 | 11.6 | 12.0 | 11.5 | 10.2 | 9.3 | 7.9 | 7.5 | 11.2 | 9.3 | 7.8 | 9.0 | 9.0 | 7.4 |
| $Na_2O$ (wt%) | 2.8 | 2.8 | 2.7 | 2.7 | 3.2 | 3.2 | 2.9 | 2.9 | 3.6 | 3.7 | 2.7 | 2.4 | 3.3 | 2.9 | 2.7 | 3.8 |
| $K_2O$ (wt%) | 0.3 | 0.3 | 0.3 | 0.3 | 0.5 | 0.5 | 0.4 | 0.4 | 1.9 | 2.1 | 1.0 | 0.9 | 1.9 | 1.2 | 1.3 | 1.9 |
| MnO (wt%) | 0.1 | 0.1 | 0.2 | 0.1 | 0.2 | 0.2 | 0.2 | 0.1 | 0.3 | 0.3 | 0.3 | 0.4 | 0.3 | 0.3 | 0.3 | 0.3 |
| $Cr_2O_3$ (wt%) | 0.1 | 0.1 | 0.1 | 0.1 | 0.0 | 0.0 | 0.1 | 0.1 | 0.0 | 0.0 | 0.0 | 0.0 | 0.0 | 0.0 | 0.0 | 0.0 |
| Total | 97.9 | 97.7 | 97.6 | 97.7 | 94.5 | 94.3 | 97.7 | 94.4 | 97.4 | 96.6 | 94.7 | 98.4 | 94.4 | 95.3 | 97.3 | 98.4 |
| $H_2O$ (wt%) | 2.84 | 2.75 | 2.6 | 2.62 | 2.78 | 2.77 | 2.7 | 2.73 | 2.07 | 2.14 | 2.54 | N.D | N.D | N.D | 2.23 | 2.27 |
| $CO_2$ ppm | 1841 | 3834 | 4148 | 3758 | 1734 | 2210 | 3986 | 4010 | 559 | 550 | 645 | N.D | N.D | N.D | 606 | 502 |
| F ppm | 473 | 216 | 205 | 204 | 468 | 470 | 233 | 239 | 560 | 545 | 594 | N.D | N.D | N.D | 514 | 680 |
| Cl ppm | 812 | 238 | 320 | 312 | 919 | 918 | 501 | 547 | 818 | 799 | 1288 | N.D | N.D | N.D | 804 | 1336 |
| S ppm | 780 | 818 | 895 | 862 | 1329 | 1359 | 951 | 1032 | 59 | 53 | 1085 | N.D | N.D | N.D | 162 | 157 |
| $H_2O/(H_2O+CO_2)$ Mol | 0.97 | 0.95 | 0.94 | 0.94 | 0.98 | 0.97 | 0.94 | 0.94 | 0.99 | 0.99 | 0.99 | - | - | - | 0.99 | 0.99 |
| Kd Fe–Mg host/MI | 0.41 | 0.40 | 0.45 | 0.44 | 0.34 | 0.36 | 0.45 | 0.44 | 0.68 | 0.69 | 0.43 | 0.54 | 0.43 | 0.45 | 0.63 | 0.68 |
| P.E.C Corrected | | | | | | | | | | | | | | | | |
| $SiO_2$ (wt%) | 50.82 | 50.60 | 49.86 | 49.79 | 46.49 | 46.55 | 49.45 | 50.96 | 51.28 | 52.37 | 47.34 | 49.83 | 50.81 | 49.93 | 51.25 | 49.20 |
| $Al_2O_3$ (wt%) | 1.86 | 1.86 | 1.85 | 1.86 | 1.91 | 1.87 | 1.89 | 1.98 | 2.55 | 2.30 | 2.01 | 2.61 | 2.25 | 2.10 | 1.78 | 2.46 |
| $TiO_2$ (wt%) | 13.92 | 13.92 | 14.23 | 14.15 | 13.60 | 13.69 | 15.84 | 13.81 | 16.18 | 15.63 | 13.45 | 14.34 | 12.74 | 13.39 | 14.52 | 15.34 |
| $Fe_2O_3$ (wt%) | 2.53 | 2.52 | 2.57 | 2.58 | 2.76 | 2.82 | 2.63 | 2.76 | 2.93 | 2.87 | 3.47 | 3.43 | 3.40 | 3.44 | 3.23 | 3.65 |
| FeO (wt%) | 7.26 | 7.32 | 7.10 | 7.19 | 8.46 | 8.49 | 7.24 | 7.68 | 6.78 | 6.61 | 9.71 | 8.73 | 9.47 | 9.45 | 7.68 | 8.43 |
| MnO (wt%) | 0.16 | 0.17 | 0.19 | 0.18 | 0.22 | 0.21 | 0.19 | 0.18 | 0.36 | 0.35 | 0.38 | 0.49 | 0.35 | 0.37 | 0.40 | 0.40 |
| MgO (wt%) | 6.76 | 6.90 | 6.56 | 6.65 | 8.01 | 8.06 | 6.29 | 6.77 | 2.91 | 2.84 | 5.43 | 4.83 | 5.06 | 5.14 | 4.12 | 3.40 |
| CaO (wt%) | 13.06 | 13.10 | 13.94 | 13.97 | 14.24 | 13.91 | 12.42 | 11.63 | 9.97 | 9.60 | 13.71 | 11.70 | 9.57 | 11.06 | 11.72 | 9.68 |
| $Na_2O$ (wt%) | 3.29 | 3.24 | 3.32 | 3.26 | 3.77 | 3.83 | 3.52 | 3.68 | 4.60 | 4.78 | 3.26 | 2.97 | 4.03 | 3.61 | 3.55 | 4.96 |
| $K_2O$ (wt%) | 0.35 | 0.36 | 0.36 | 0.37 | 0.54 | 0.55 | 0.53 | 0.55 | 2.45 | 2.65 | 1.23 | 1.07 | 2.32 | 1.52 | 1.75 | 2.49 |
| Total | 100 | 100 | 100 | 100 | 100 | 100 | 100 | 100 | 100 | 100 | 100 | 100 | 100 | 100 | 100 | 100 |
| Mg# | 62.39 | 62.69 | 62.22 | 62.22 | 62.79 | 62.83 | 60.77 | 61.10 | 43.33 | 43.34 | 49.92 | 49.67 | 48.77 | 49.20 | 48.90 | 41.78 |
| FeOt (wt%) | 9.53 | 9.59 | 9.42 | 9.52 | 10.94 | 11.03 | 9.61 | 10.16 | 9.42 | 9.19 | 12.83 | 11.81 | 12.53 | 12.55 | 10.58 | 11.71 |
| $H_2O$ (wt%) | 3.26 | 3.13 | 3.07 | 3.08 | 3.11 | 3.14 | 3.19 | 3.21 | 2.55 | 2.64 | 2.95 | N.D | N.D | N.D | 2.82 | 2.90 |

**Table 2** (continued)

| Period | Tholeiite | Tholeiite | Tholeiite | Tholeiite | Tholeiite | Tholeiite | Tholeiite | Tholeiite | Ellittico | Ellittico | Ellittico | Ellittico | Ellittico | Ellittico | Ellittico | Ellittico |
|---|---|---|---|---|---|---|---|---|---|---|---|---|---|---|---|---|
| Sample | ET4 | ET4 | ET4 | ET4 | ET4 | ET4 | ET4 | ET4 | ET 51 | ET 51 | ET 51 | ET 51 | ET 51 | ET 51 | ET 51 | ET 51 |
| Host crystal | Ol 1 | Ol 1 | Ol 1 | Ol 1 | Ol 2 | Ol 2 | Ol 4 | Ol 4 | Ol 5 | Ol 5 | Ol 6 | Ol 6 | Ol 6 | Ol 6 | Ol 7 | Ol 8 |
| DataSet/Point | 1/1 | 1/2 | 5/1 | 5/2 | 7/1 | 8/1 | 15/1 | 17/1 | 18/1 | 18/2 | 21/1 | 24/1 | 26/1 | 28/1 | 31/1 | 34/1 |
| $CO_2$ ppm | 2112 | 4370 | 4900 | 4418 | 1937 | 2509 | 4708 | 4721 | 690 | 677 | 748 | N.D | N.D | N.D | 766 | 640 |
| F ppm | 473 | 216 | 205 | 204 | 468 | 470 | 233 | 239 | 560 | 545 | 594 | N.D | N.D | N.D | 514 | 680 |
| Cl ppm | 932 | 271 | 378 | 367 | 1027 | 1042 | 592 | 644 | 1009 | 984 | 1494 | N.D | N.D | N.D | 1016 | 1704 |
| S ppm | 895 | 932 | 1057 | 1013 | 1485 | 1543 | 1123 | 1215 | 73 | 65 | 1258 | N.D | N.D | N.D | 205 | 200 |
| Ol. Add (%) | −12.95 | −12.33 | −15.4 | −15 | −10.23 | −11.59 | −15.41 | −14.66 | −18.9 | −18.6 | −13.4 | −18.9 | −13.5 | −14.5 | −20.8 | −21.8 |
| KD | 0.31 | 0.31 | 0.31 | 0.31 | 0.29 | 0.29 | 0.30 | 0.31 | 0.28 | 0.28 | 0.30 | 0.30 | 0.29 | 0.29 | 0.30 | 0.29 |

| Period | Ellittico | Rec. Mong | Rec. Mong | Rec. Mong | Rec. Mong | 2015 | 2015 | 2015 | 2015 | 2015 | 2015 | 2015 | 2015 | 2015 | 2015 | 2015 | 2015 |
|---|---|---|---|---|---|---|---|---|---|---|---|---|---|---|---|---|---|
| Sample | ET 51 | ET 45 | ET 45 | ET 45 | ET 45 | NEC | NEC | NEC | SEX | SEX | SEX | SEX | CC | CC | CC | CC | CC | CC |
| Host crystal | Ol 8 | Ol 11 | Ol 11 | Ol 12 | Ol 12 | Ol 1 | Ol 4 | Ol 6 | Ol 8 | Ol 8 | Ol 8 | Ol 10 | Ol 14 | Ol 14 | Ol 15 | Ol 16 | Ol 16 | Ol 18 |
| DataSet/Point | 34/2 | 46/1 | 47/1 | 48/1 | 50/1 | 64/1 | 72/1 | 82/1 | 90/1 | 94/1 | 98/1 | 103/1 | 106/1 | 109/1 | 110/1 | 114/1 | 117/1 | 121/1 |
| $SiO_2$ (wt%) | 46.5 | 47.3 | 48.0 | 46.5 | 46.6 | 46.8 | 44.8 | 43.9 | 45.7 | 45.8 | 45.9 | 45.8 | 46.0 | 41.5 | 45.7 | 44.1 | 46.2 | 43.1 |
| $Al_2O_3$(wt%) | 10.8 | 11.8 | 11.8 | 12.3 | 12.8 | 11.6 | 10.3 | 11.1 | 10.1 | 10.0 | 11.2 | 10.8 | 9.9 | 12.5 | 10.9 | 11.4 | 10.8 | 13.7 |
| $TiO_2$ (wt%) | 1.9 | 1.5 | 1.5 | 1.9 | 1.9 | 2.0 | 1.3 | 1.4 | 1.5 | 1.5 | 1.4 | 1.6 | 1.5 | 1.7 | 1.5 | 1.8 | 1.3 | 2.0 |
| FeOT (wt%) | 12.7 | 9.2 | 9.2 | 10.9 | 11.1 | 15.2 | 11.2 | 11.4 | 13.0 | 12.9 | 12.1 | 11.9 | 12.1 | 12.7 | 13.0 | 13.3 | 13.6 | 11.2 |
| MgO (wt%) | 12.2 | 12.1 | 11.8 | 10.6 | 11.4 | 9.0 | 7.3 | 12.5 | 11.0 | 11.7 | 10.9 | 11.3 | 11.1 | 7.9 | 10.5 | 9.4 | 10.8 | 6.0 |
| CaO (wt%) | 7.4 | 9.2 | 9.3 | 8.7 | 8.2 | 9.6 | 8.6 | 10.8 | 10.3 | 10.1 | 10.2 | 11.2 | 11.3 | 12.6 | 9.7 | 9.1 | 8.6 | 11.4 |
| $Na_2O$ (wt%) | 3.8 | 4.0 | 3.8 | 3.8 | 3.8 | 4.0 | 2.4 | 4.1 | 3.7 | 3.5 | 3.4 | 3.4 | 3.2 | 2.8 | 3.8 | 3.5 | 3.6 | 3.5 |
| $K_2O$ (wt%) | 1.9 | 1.8 | 1.7 | 1.7 | 1.8 | 2.4 | 2.1 | 2.0 | 2.1 | 2.1 | 1.9 | 1.8 | 1.9 | 1.4 | 2.0 | 2.0 | 2.0 | 1.4 |
| MnO (wt%) | 0.3 | 0.3 | 0.3 | 0.4 | 0.4 | 0.3 | 0.3 | 0.3 | 0.3 | 0.3 | 0.3 | 0.2 | 0.2 | 0.3 | 0.3 | 0.3 | 0.3 | 0.2 |
| $Cr_2O_3$ (wt%) | 0.0 | 0.0 | 0.0 | 0.0 | 0.0 | 0.0 | 0.0 | 0.0 | 0.0 | 0.0 | 0.0 | 0.0 | 0.1 | 0.0 | 0.0 | 0.0 | 0.0 | 0.0 |
| Total | 97.5 | 97.2 | 97.5 | 96.7 | 97.8 | 100.9 | 88.3 | 97.3 | 97.6 | 98.0 | 97.1 | 98.1 | 97.2 | 93.4 | 97.3 | 95.0 | 97.3 | 92.3 |
| $H_2O$ (wt%) | 2.3 | 2.2 | 2.16 | 2.19 | 1.93 | 5.27 | 4.07 | 4.04 | 4.91 | 4.33 | N.D | 4.07 | 3.95 | N.D | 4.05 | 4.11 | 3.95 | 4.26 |
| $CO_2$ ppm | 500 | 445 | 483 | 685 | 416 | 381 | 2353 | 8151 | 730 | 282 | N.D | 412 | 285 | N.D | 283 | 318 | 239 | 476 |
| F ppm | 697 | 520 | 531 | 551 | 574 | 517 | 305 | 132 | 597 | 492 | N.D | 500 | 618 | N.D | 640 | 532 | 537 | 520 |
| Cl ppm | 1382 | 1071 | 1094 | 1082 | 1362 | 1092 | 438 | 213 | 1022 | 928 | N.D | 955 | 686 | N.D | 1212 | 948 | 1020 | 1400 |
| S ppm | 160 | 43 | 38 | 32 | 144 | 379 | 406 | 934 | 562 | 15 | N.D | 24 | 174 | N.D | 248 | 345 | 545 | 2042 |
| $H_2O/(H_2O+CO_2)$ Mol | 0.99 | 0.99 | 0.99 | 0.99 | 0.99 | 1.00 | 0.98 | 0.92 | 0.99 | 1.00 | - | 1.00 | 1.00 | #DIV/0! | 1.00 | 1.00 | 1.00 | 1.00 |
| Kd Fe–Mg host/MI | 0.68 | 0.65 | 0.64 | 0.67 | 0.71 | 0.51 | 0.41 | 0.26 | 0.30 | 0.32 | 0.32 | 0.40 | 0.42 | 0.29 | 0.44 | 0.44 | 0.49 | 0.21 |
| P.E.C Corrected | | | | | | | | | | | | | | | | | | |
| $SiO_2$ (wt%) | 49.80 | 50.71 | 51.35 | 49.95 | 49.59 | 47.61 | 51.88 | 45.13 | 47.16 | 47.26 | 47.82 | 47.61 | 48.43 | 44.57 | 48.04 | 47.34 | 48.94 | 46.33 |
| $Al_2O_3$ (wt%) | 2.45 | 1.89 | 1.94 | 2.43 | 2.39 | 2.35 | 1.65 | 1.49 | 1.64 | 1.63 | 1.55 | 1.94 | 1.81 | 1.94 | 1.75 | 2.19 | 1.63 | 2.06 |

**Table 2** (continued)

| Period | Ellittico | Rec. Mong | Rec. Mong | Rec. Mong | Rec. Mong | 2015 | 2015 | 2015 | 2015 | 2015 | 2015 | 2015 | 2015 | 2015 | 2015 | 2015 | 2015 | 2015 |
|---|---|---|---|---|---|---|---|---|---|---|---|---|---|---|---|---|---|---|
| Sample | ET 51 | ET 45 | ET 45 | ET 45 | ET 45 | NEC | NEC | NEC | SEX | SEX | SEX | SEX | CC | CC | CC | CC | CC | CC |
| Host crystal | Ol 8 | Ol 11 | Ol 11 | Ol 12 | Ol 12 | Ol 1 | Ol 4 | Ol 6 | Ol 8 | Ol 8 | Ol 8 | Ol 10 | Ol 14 | Ol 14 | Ol 15 | Ol 16 | Ol 16 | Ol 18 |
| DataSet/Point | 34/2 | 46/1 | 47/1 | 48/1 | 50/1 | 64/1 | 72/1 | 82/1 | 90/1 | 94/1 | 98/1 | 103/1 | 106/1 | 109/1 | 110/1 | 114/1 | 117/1 | 121/1 |
| $TiO_2$ (wt%) | 14.25 | 15.30 | 15.07 | 15.68 | 16.48 | 13.43 | 12.97 | 11.82 | 11.05 | 11.19 | 12.66 | 12.65 | 11.78 | 14.24 | 13.06 | 13.88 | 13.28 | 14.42 |
| $Fe_2O_3$ (wt%) | 3.71 | 2.64 | 2.60 | 3.10 | 3.16 | 3.91 | 3.13 | 2.70 | 3.15 | 3.21 | 3.04 | 3.10 | 3.22 | 3.20 | 3.45 | 3.60 | 3.72 | 2.62 |
| FeO (wt%) | 8.59 | 6.21 | 6.16 | 7.26 | 7.23 | 10.20 | 9.01 | 9.25 | 10.33 | 10.22 | 9.56 | 8.90 | 9.08 | 10.39 | 9.58 | 10.01 | 9.84 | 9.91 |
| MnO (wt%) | 0.43 | 0.42 | 0.41 | 0.50 | 0.50 | 0.34 | 0.38 | 0.28 | 0.29 | 0.30 | 0.28 | 0.29 | 0.27 | 0.29 | 0.30 | 0.38 | 0.36 | 0.26 |
| MgO (wt%) | 3.48 | 3.43 | 3.44 | 2.98 | 2.94 | 3.60 | 4.51 | 11.33 | 8.83 | 8.66 | 7.62 | 6.21 | 5.82 | 6.21 | 5.23 | 4.81 | 4.75 | 7.36 |
| CaO (wt%) | 9.80 | 11.89 | 11.91 | 11.07 | 10.56 | 11.14 | 10.76 | 11.49 | 11.21 | 11.25 | 11.51 | 13.15 | 13.56 | 14.34 | 11.66 | 11.07 | 10.56 | 11.95 |
| $Na_2O$ (wt%) | 5.05 | 5.13 | 4.89 | 4.81 | 4.83 | 4.66 | 3.05 | 4.38 | 4.06 | 3.93 | 3.85 | 3.99 | 3.78 | 3.19 | 4.51 | 4.25 | 4.43 | 3.66 |
| $K_2O$ (wt%) | 2.46 | 2.37 | 2.23 | 2.23 | 2.32 | 2.76 | 2.65 | 2.13 | 2.28 | 2.37 | 2.10 | 2.17 | 2.24 | 1.64 | 2.42 | 2.46 | 2.50 | 1.42 |
| Total | 100 | 100 | 100 | 100 | 100 | 100 | 100 | 100 | 100 | 100 | 100 | 100 | 100 | 100 | 100 | 100 | 100 | 100 |
| Mg# | 41.91 | 49.60 | 49.88 | 42.25 | 42.01 | 38.61 | 47.14 | 68.58 | 60.36 | 60.15 | 58.68 | 55.43 | 53.31 | 51.57 | 49.29 | 46.11 | 46.27 | 56.97 |
| FeOt (wt%) | 11.92 | 8.58 | 8.50 | 10.05 | 10.08 | 13.72 | 11.82 | 11.68 | 13.16 | 13.10 | 12.30 | 11.69 | 11.98 | 13.27 | 12.69 | 13.25 | 13.18 | 12.27 |
| $H_2O$ (wt%) | 2.94 | 2.75 | 2.68 | 2.70 | 2.42 | 6.14 | 4.51 | 4.20 | 5.24 | 4.72 | N.D | 4.68 | 4.57 | N.D | 4.70 | 4.73 | 4.70 | 4.15 |
| $CO_2$ ppm | 639 | 557 | 600 | 845 | 523 | 444 | 2605 | 8474 | 779 | 308 | N.D | 473 | 330 | N.D | 329 | 366 | 284 | 464 |
| F ppm | 697 | 520 | 531 | 551 | 574 | 517 | 305 | 132 | 597 | 492 | N.D | 500 | 618 | N.D | 640 | 532 | 537 | 520 |
| Cl ppm | 1766 | 1341 | 1360 | 1334 | 1711 | 1272 | 485 | 221 | 1090 | 1012 | N.D | 1097 | 794 | N.D | 1407 | 1091 | 1214 | 1365 |
| S ppm | 204 | 54 | 47 | 39 | 181 | 441 | 449 | 971 | 599 | 16 | N.D | 28 | 201 | N.D | 288 | 397 | 649 | 1992 |
| Ol. Add (%) | –21.8 | –20.05 | –19.51 | –18.74 | –20.4 | –15 | –8.95 | –3.87 | –6.41 | –8.51 | –9.08 | –13.27 | –13.82 | –5.73 | –14.1 | –13.01 | –16.22 | 2.45 |
| KD | 0.29 | 0.27 | 0.28 | 0.28 | 0.28 | 0.31 | 0.32 | 0.29 | 0.30 | 0.30 | 0.28 | 0.29 | 0.30 | 0.28 | 0.29 | 0.30 | 0.30 | 0.30 |

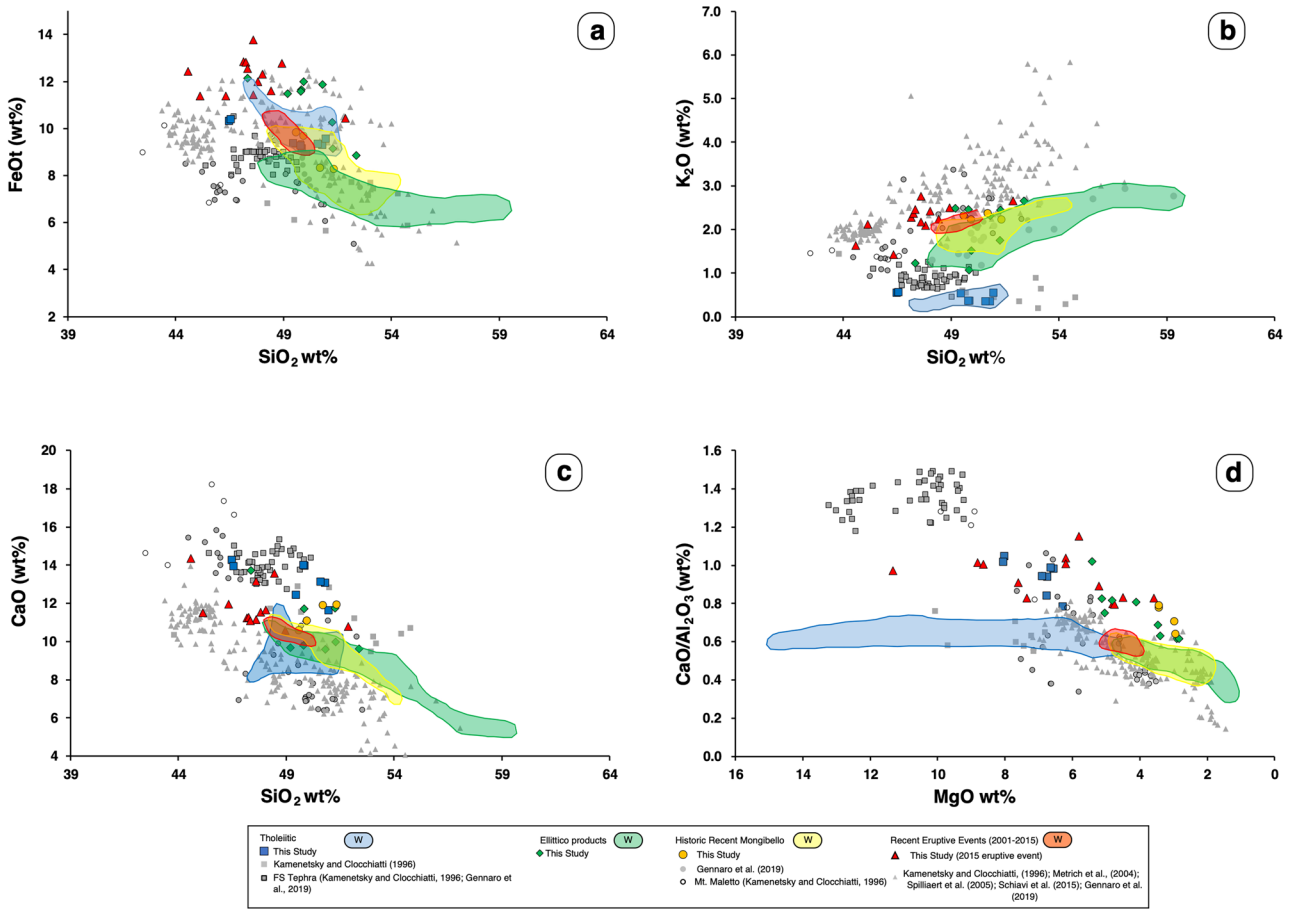


**Fig. 4** Harker variation diagrams showing major element composition of studied MIs and bibliographic data: **a** $SiO_2$ vs FeOt; **b** $SiO_2$ vs $K_2O$; **c** $SiO_2$ vs CaO and **d** MgO vs $CaO/Al_2O_3$

data shows a less noticeable trend, keeping the $CaO/Al_2O_3$ almost constant at decreasing MgO.

Concerning the Fe–Mg partitioning between MIs and the host olivine during the homogenization procedure, a general disequilibrium is observed between the host-olivine and studied MI. The $^{Fe-Mg}Kd_{Host\text{-}MIs}$ value is considered at equilibrium when comprised in the range of $0.30 \pm 0.03$ (Roeder and Emslie 1970). Except for two MIs of the 2015 eruption, embedded in a $Fo_{83}$ olivine, the majority of MIs lies above the equilibrium range, indicating that they could be more evolved than their host olivine or that overheating occurred during the homogenization experiments (Fig. 5a-b, Table 1).

## Post-entrapment modifications and correction

MIs can preserve a record of changes in the magma composition (i.e. crystal fractionation, magma mixing and degassing) or may record magma heterogeneities, if trapped at the same time at different location (Wallace et al. 2021).

However, information in MIs can be obscured by post-entrapment modifications which includes: (i) edge crystallization of the host crystal; (ii) formation of a vapor phase and (iii) elemental diffusion loss or gain ($Fe^{2+}$ and/or $H^+$). A major focus of any MIs study is to recognize and correct for the effect of various post-entrapment processes.

The available dataset on major element geochemistry of olivine-hosted MIs from Mt. Etna spans over a wide range of magma compositions that is significantly larger than that of the erupted lavas (Metrich et al. 2004; Schiavi et al. 2015; Gennaro et al. 2019). Our geochemical data on MIs are in general agreement with literature trends, however, in this section, we explore the possibility that each series (i.e. tholeiitic and alkaline) derives from a distinct parental magma and that variations in the physical–chemical conditions of crystallization at crustal depth may explain most of the observed compositional variations. The broad variation in MIs composition could in fact results from the diversity of the methodological approaches adopted by different authors before and during the geochemical analyses, resulting from the absence of a shared homogenization and analytical protocol. Apart from this study, the available MIs data were mostly obtained after a high-temperature

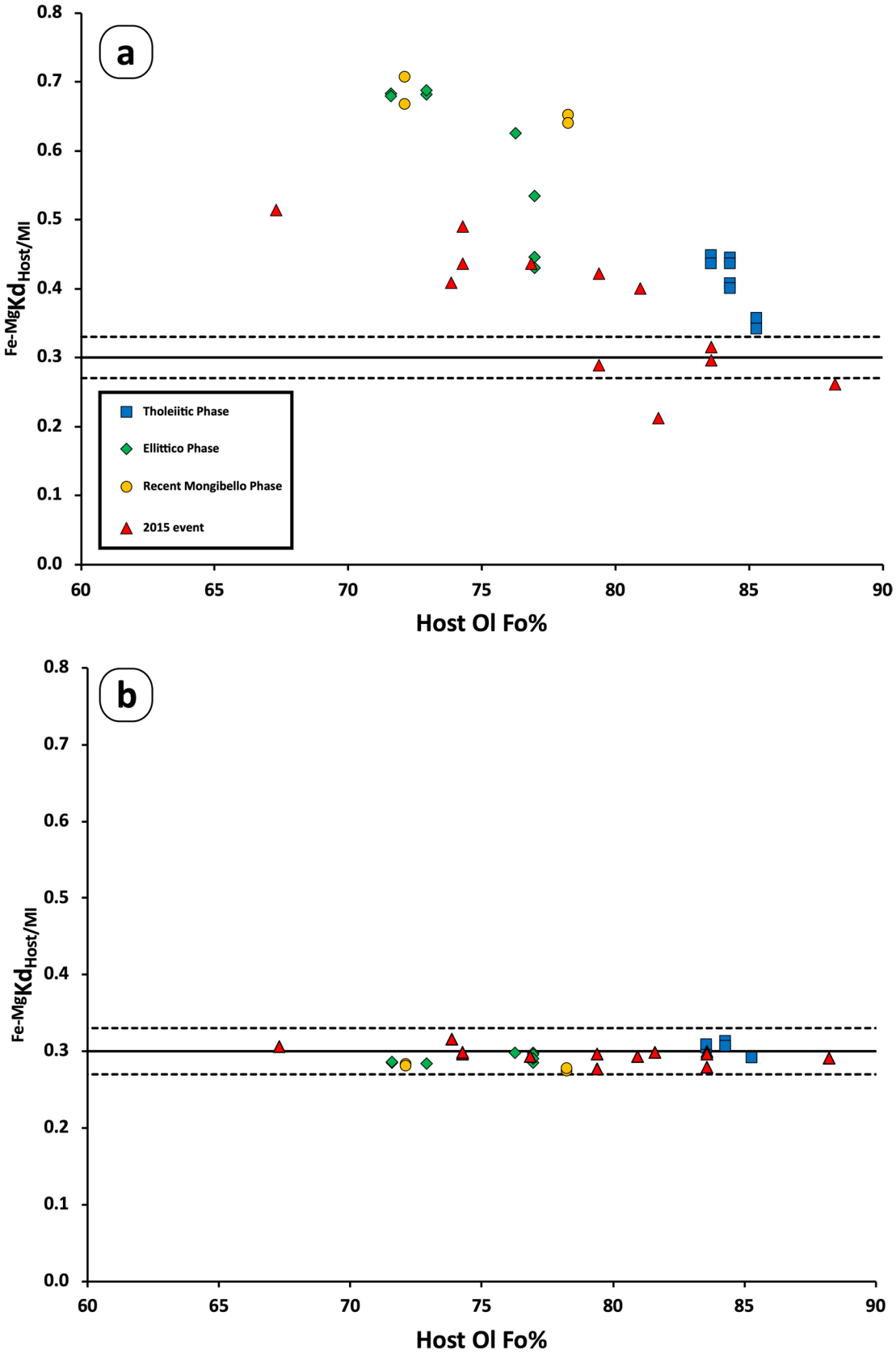


**Fig. 5** $^{Fe-Mg}Kd_{Host/MI}$ vs forsterite (Fo) content of host olivine in original MI **a** and after post-entrapment correction **b**, **c** Estimated entrapment pressure (P) vs Fo content of host olivine

homogenization procedure at 1-atm, eventually followed by post-entrapment correction (PEC), aiming to re-dissolve the daughter crystals and the vapor phase in the melt and to reduce any MI-Host Fe–Mg exchange as consequence of host crystallization or melting at the crystal-MI interface. In other cases, volatile-focused studies preferred to carefully select some naturally quenched MIs from tephra, advocating that high-temperature homogenization procedure itself could alter the original MI composition, by enhancing elemental lost through diffusion and host-crystal assimilation and/or crystallization (Kamenetsky et al. 2007).

Since studied MIs show an evident disequilibrium having $^{Fe-Mg}Kd_{Host\text{-}Mi} > 0.33$ we have decided to perform a PEC to achieve the MI-host chemical equilibrium. Moreover, to better compare our MIs analyses with those reported in the literature and obtained with different analytical and experimental methods, the latter compositions have been treated uniformly by considering all Fe expressed as $FeO_T$ and normalized to 100 on anhydrous bases.

All analyzed MIs were thus re-equilibrated by applying the MIMic Pyhton script designed and described in Rasmussen et al. (2020). The applied Fe–Mg partition coefficient is calculated using the model of Toplis (2005) and corrected (for each calculation step) for the estimated pressure obtained from the $H_2O$ and $CO_2$ concentration following the solubility model of VolatileCalc (Newman and Lowenstern 2002). The melt temperature is estimated by means of the olivine-liquid thermometer (Eq. 4) of Putirka et al. (2007). The MIMiC allows the user to decide whether the $Fe^{3+}/Fe^T$ varies during the correction ($Fe_2O_3$ treated as an incompatible element) or not. Calculations performed in this study were made by keeping the $Fe^{3+}/Fe^T$ constant at 0.2, which is a reasonable value in accordance with the expected $fO_2$ of Mt. Etna magmatic system (Giacomoni et al. 2014). We have allowed the MIMiC script to correct for Fe–Mg exchange since we observed a diffusive rim characterized by a Fo gradient approaching the MI-Host edge. Fe–Mg exchange described the process of Fe-Loss from a MI following PEC or Fe-gain following PEM (Danyushevsky et al. 2000; Rasmussen et al. 2020).

Since most of studied MIs presented here have a $^{Fe-Mg}Kd_{Host\text{-}MI} > 0.33$, equilibrium was achieved by subtracting (PEM) a variable amount of host-olivine ranging from 3 to 21%; only for a unique MI with $^{Fe-Mg}Kd_{Host\text{-}Mi} < 0.33$ equilibrium was obtained by adding (PEC) 2% of equilibrium olivine (Fig. 5a-b). The causes behind the initial disequilibrium between the MIs and the host olivine could be ascribed to the homogenization temperature above the Ol liquidus (over heating) inducing the assimilation of the host-olivine. This process affected mostly low Fo olivines, gradually decreasing at higher Fo content.

## Volatile content of melt inclusions

The volatile content of studied MIs varies significantly; $H_2O$ concentration ranges between 2.42 wt% to 6.14 wt% and $CO_2$ content vary between 308 and 8874 ppm (Table 2). The highest $H_2O$ concentration measured in a 2015 MI (6.14 wt%) is comparable with that measured in the FS Tephra (up to 6 wt%) by Gennaro et al. (2019) and is higher than the previously analyses of FS tephra by Kamenetzky et al. (2007) (2.6–3.8 wt%).

The highest $CO_2$ value is found in a sample from the 2015 lava (8874 ppm), and exceeds the maximum values obtained by Gennaro et al. (2019) for the FS tephra (6015 ppm). $CO_2$ contents in samples from the Tholeiitic phase range from 1937 to 4900 ppm while more recent samples from Ellittico and Recent Mongibello plot in a restricted range between 523 and 845 ppm. The broad range in $CO_2$ abundances observed in each phase indicates an important $CO_2$-loss during magma ascent and decompression. The resulting $H_2O/(H_2O+CO_2)$ molar ratio ranges from 0.92 to 1 (Fig. 6). Inside this large range, common to all alkaline samples, Tholeiitic inclusions plot in a range comprised between 0.94 and 0.98; almost constant 0.99 for Ellittico and Historic Mongibello and ranges from 0.92 to 1 in in 2015 MIs.

The F and Cl content are positively correlated and range from 132 to 697 ppm and from 221 to 1766 ppm respectively (Fig. 7a-b), suggesting a common behaviour of these volatile species during magma ascent and degassing. The concentration of S (Fig. 7c) is also extremely variable, ranging from 16 to 1992 ppm with the highest content measured in the recent 2015 products. F, Cl and S do not show any significant correlation with $H_2O$ and/or $CO_2$.

The relationship between the Fo content of host-Ol and the concentration in volatiles of the MIs is showed in Fig. 8a-c. Mis from the recent 2015 eruptive event have a significantly higher $H_2O$ content, despite sharing a comparable range in Fo with the other studied volcanic phase (Fig. 8a). Most of studied MIs show a quite low $CO_2$ concentration irrespective of the Fo content of host Ol, further evidencing the effect of the low solubility of $CO_2$ in the etnean magmatic system. The higher $CO_2$ content was measured in the 2015 MIs with Fo88 and in few inclusions from the Tholeiitic phase which are commonly more Fo-rich.

The F and Cl contents (Fig. 8c) vary significantly, and they are generally negatively correlated with the host Fo. This is consistent with the higher solubility of both F and Cl at lower

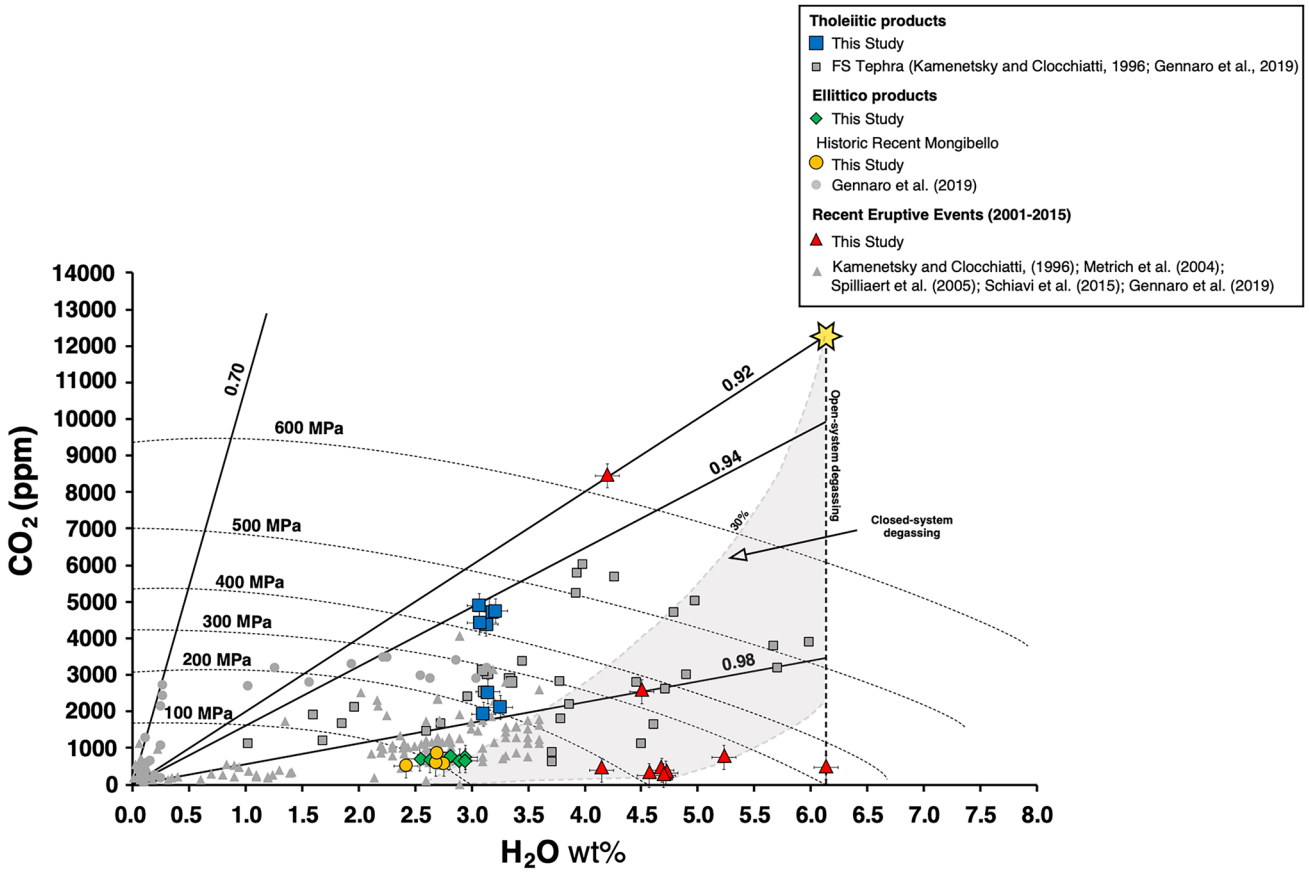


**Fig. 6** $CO_2$ vs $H_2O$ of studied and bibliographic MIs. Solid lines reproduce possible $H_2O/(H_2O+CO_2)$ molar ratios representative of initial undegassed magmas. Isobars were calculated at 1200 °C by means of the solubility model of Iacono Marziano et al. (2012). The depths (below crater levels) have been estimated from the crustal density from Corsaro and Pompilio (2004). The grey areas are obtained simulating the degassing path starting from the measured highest $CO_2$ content of 8151 ppm and 6.3 wt% $H_2O$, leading to the estimated 12,250 ppm on the basis of the $H_2O/(H_2O+CO_2)$ mol = 0.92. The grey dotted lines and area represent the open- and closed-system degassing paths (up to 30% of excess fluid phase), simulated with VolatileCalc

pressure, hence testifying to some degree of differentiation during magma ascent.

## Discussion

### Volatile content of undifferentiated melts

The entrapment pressure of MIs has been estimated by using the $H_2O$-$CO_2$ solubility model of Iacono Marziano et al. (2012), calibrated for alkaline magmas between 900 °C and 1200 °C. By using this model, the estimated $H_2O$ and $CO_2$ contents are calculated at volatile saturation and hence considered as minimum entrapment pressures. Results (Fig. 6) show that MIs were trapped at pressures ranging between 610 ± 50 MPa and 85 ± 50 MPa, corresponding to an estimated depth from 16 km below summit craters to 1 km below summit craters, considering an average crustal density of 2.6 g/cm$^3$ (Corsaro and Pompilio 2004). The 2015 inclusion containing 8474 ppm $CO_2$ and 4.20 wt% $H_2O$ is the deepest and, given the low $H_2O/(H_2O+CO_2)$ molar ratio of 0.92 and the high Fo content of its host olivine ($Fo_{88}$), it could be considered as the most representative of the pristine volatile content of alkaline primary magmas feeding the current Mt. Etna activity. The remaining MIs of the 2015 eruption with $H_2O$ concentration up to 6.14 wt% record different degree of $CO_2$ degassing during magma ascent in an open-system regime. Similarly, all studied MIs from Ellittico and Recent Mongibello underwent significant degassing of both $H_2O$ and $CO_2$ before being trapped at shallow pressure (< 110 MPa). Several MIs from the tholeiitic phase still preserve a quite high $CO_2$ concentration (up to 4900 ppm) and a $H_2O/(H_2O+CO_2)$ molar ratio of 0.94, resulting in an estimated entrapment pressures ranging from 569 ± 50 MPa to 203 ± 30 MPa. On the other hand, some tholeiitic MIs show an higher $H_2O/(H_2O+CO_2)$ molar ratio of 0.98 that, considered their constant $H_2O$ concentration of 3.2 wt% but

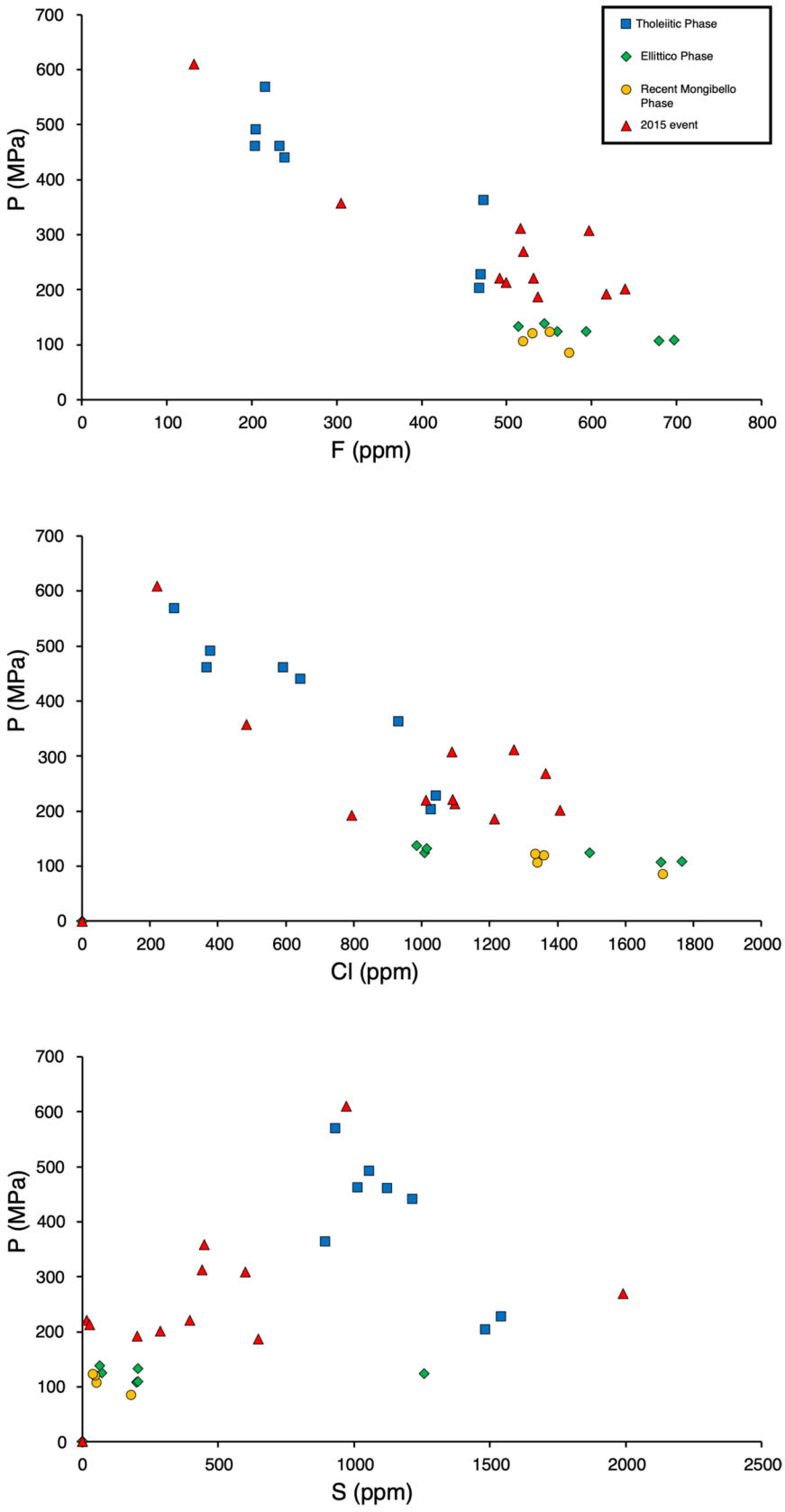


**Fig. 7** F **a**, Cl **b** and S **c** content of studied MIs versus the entrapment pressure calculated using the $H_2O$ and $CO_2$ content inferred using the solubility model of Iacono Marziano et al. (2012)

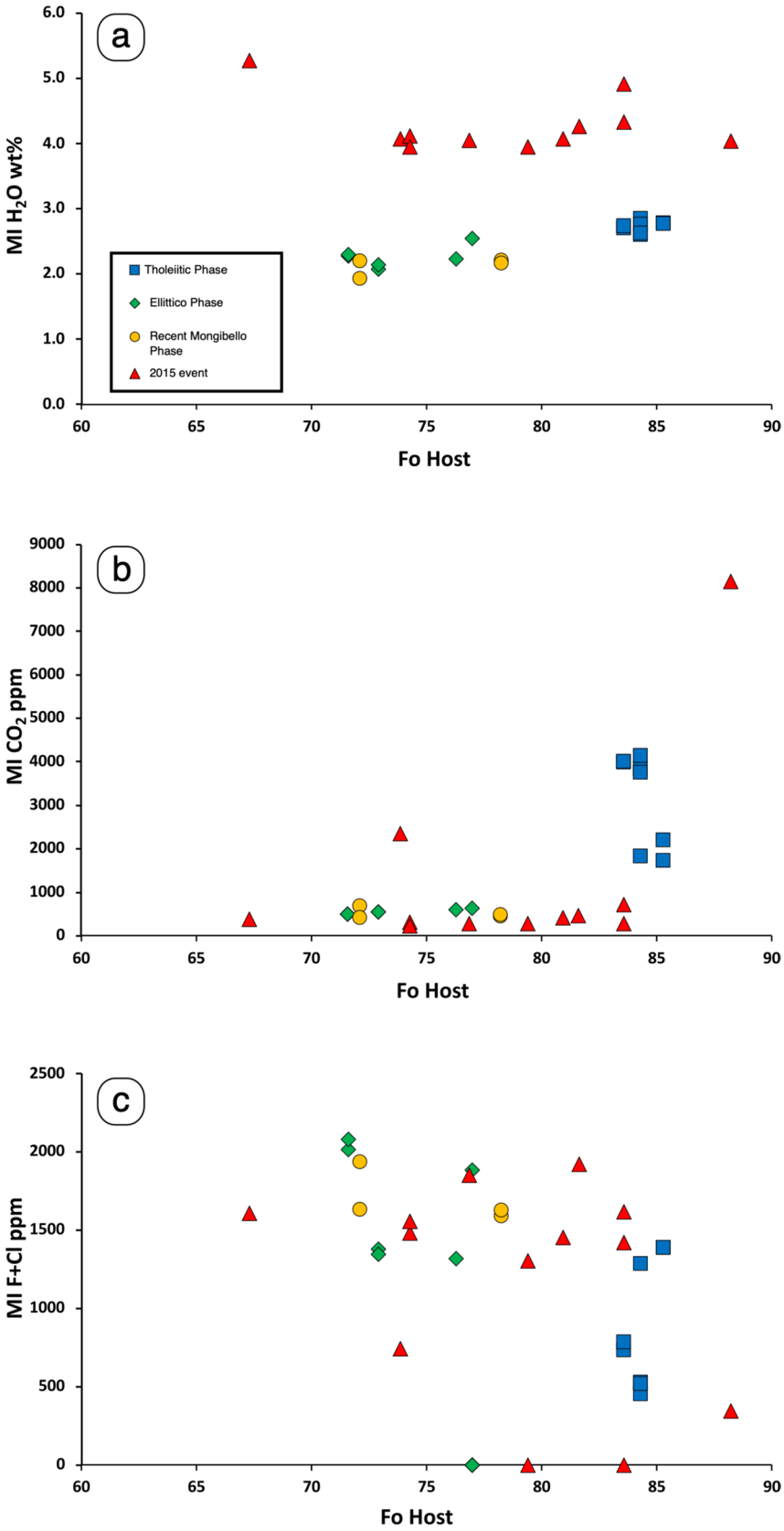


**Fig. 8** $H_2O$ **a**, $CO_2$ **b** and F + Cl **c** versus host olivine Fo content

significantly lower $CO_2$, suggests that they reasonably underwent to $CO_2$ degassing during ascent.

However, the high Fo contents of host Ol ($Fo_{83-86}$) of the whole tholeiitic suite of samples, points to consider the measured volatile content with $H_2O/(H_2O+CO_2)$ molar ratio of 0.94 close to the pristine concentration in the primary magma. The positive correlation between estimated entrapment pressure and host-olivine Fo content (Fig. 5a and b, c) supports the quality of the dataset, although, the estimated entrapment pressure is systematically lower than the pressure derived from Ol and Cpx thermobarometry (Giacomoni et al. 2018; 2020). The mismatch could be caused by two concomitant processes: (i) disequilibrium crystallization which affected the thermobarometric estimates and (ii) MIs degassing and subsequent underestimation of the crystallization pressure. In this context, the ascent of the host olivine in the magma and MIs entrapment could occur at a significant higher speed than the olivine-melt re-equilibration.

The large variability in $H_2O$ and $CO_2$ reveals different degassing patterns; the modelling reproduces the observed concentration in MIs (Fig. 6) if an open-system degassing regime is assumed to exsolve $CO_2$ at significantly higher pressure than $H_2O$ (600 MPa).

The recognized MI containing 6.1 wt% $H_2O$ in recent 2015 alkaline products lead to suppose that its measured 440 ppm $CO_2$ is strongly affected by degassing. Aiming to estimate the pristine $H_2O$ and $CO_2$ content of recent alkaline melts, a maximum content of 12,250 ppm $CO_2$ can be reconstructed assuming that this MI had a pristine $H_2O/(H_2O+CO_2)$ molar ratio of 0.92 (Fig. 6) and suffered $CO_2$ loss in an open-conduit regime.

In this scenario, the majority of studied MIs can be interpreted as being trapped during magma evolution in an open -system regime, with very few inclusions plotting along isopleth.

When compared to bibliographic data (Gennaro et al. 2019; 2020), the overall $H_2O$ versus $CO_2$ contents of melt inclusions reveals a broader variability with an outstanding high volatile content in primary magmas (up to 6 wt% $H_2O$ and 10,000 ppm $CO_2$). Moreover, the $H_2O/(H_2O+CO_2)$ mol ratio in $CO_2$-rich inclusions, apparently decreases from 0.94 in sub-alkaline inclusions from the tholeiitic phase, to 0.92 in MIs from the 2015 eruptive phase.

The observed negative correlation between calculated entrapment pressure and F and Cl contents confirms the higher solubility of halogens with respect to $H_2O$ and $CO_2$ (Dalou and Mysen 2015). In this context, the 0.92 $H_2O/(H_2O+CO_2)$ mol in MIs from the 2015 eruption should represent the primary content with 132 ppm F and 221 ppm Cl. With decreasing pressure, the F and Cl contents are enriched due to decompression-driven crystal fractionation, reaching 697 ppm F and 1992 ppm Cl (Fig. 7a-b).

## Fractionation modelling

Fractional crystallization modelling was performed using Rhyolite-MELTs (Gualda et al. 2012) starting from two parental compositions: P1, representing a tholeiitic parental melt and P2, representing a parental basanitic melt for the alkaline series. The choice of these starting points results from the observation of a significant compositional gap between early tholeiitic products and subsequent and more voluminous alkaline products; this compositional shift occurred in a very short time span (~40 ka; Tanguy et al. 1997; Branca et al. 2011). Composition P1 is derived from a MI embedded in a $Fo_{89}$ Ol of the FS Tephra from Gennaro et al. (2019) while composition P2 is derived from a MI embedded in a $Fo_{88}$ Ol from the 2015 eruption. Both selected MIs show primitive geochemical features with $SiO_2$, MgO and $CaO/Al_2O_3$ varying from 45.41 wt% to 44.39 wt%, 9.95 wt% to 8.49 wt%, and from 1.40 to 1.00 wt% respectively. Simulations were performed with 4 wt% of dissolved $H_2O$ and 6000 ppm $CO_2$ in the starting melts which can be reasonably assumed as average values for the volatile contents.

Simulations were performed in two-steps: the first at pressures decreasing from 600 to 400 MPa and temperatures from 1300 °C to 1200 °C; the second step at pressures decreasing from 400 to 50 MPa and from 1200 °C to 1000 °C. Modelling was initially made at FMQ + 1.5, in agreement with the estimation of Giacomoni et al. (2014) but was also increased up to FMQ + 3, covering the range of previous estimates (Kamenetsky and Clocchiatti 1996; Mollo et al. 2015; Gennaro et al. 2020); results are shown in Fig. 9.

Simulations starting from composition P1 reproduce a sub-alkaline tholeiitic liquid line of descent, characterized by a moderate decrease in FeOt and CaO. This trend reflects the scarcity of crystallizing clinopyroxene in the first step of simulation, which is indeed characterized by olivine + Cr-spinel. In the second step, there is a shift in the fractionating assemblage from Cr-Sp to Fe-Ti Mt. Plagioclase stability is strongly reduced by the high $H_2O$ content of the melts and restricted to $P < 100$ MPa and $T < 1100$ °C, confirming the results of Giacomoni et al. (2014). Simulations starting from composition P2 reproduce most of the observed MIs along an alkaline liquid line of descent, for which the first stage of crystallization is characterized by an almost cotectic crystallization of Ol and Cpx at 500 MPa and by the unique presence of Fe-Ti oxide. The liquid fractionation at shallower depths is constrained by the stability of clinopyroxene, Ti-magnetite and plagioclase.

Simulations confirm that a variable fractionation degree (F) ranging between 15 and 25% is needed to account for the composition of most erupted melts. The effect of increasing $fO_2$ from FMQ + 1.5 to FMQ + 3 is comparable in both simulations; $fO_2$ enlarges the oxide stability (Cr-Sp in P1

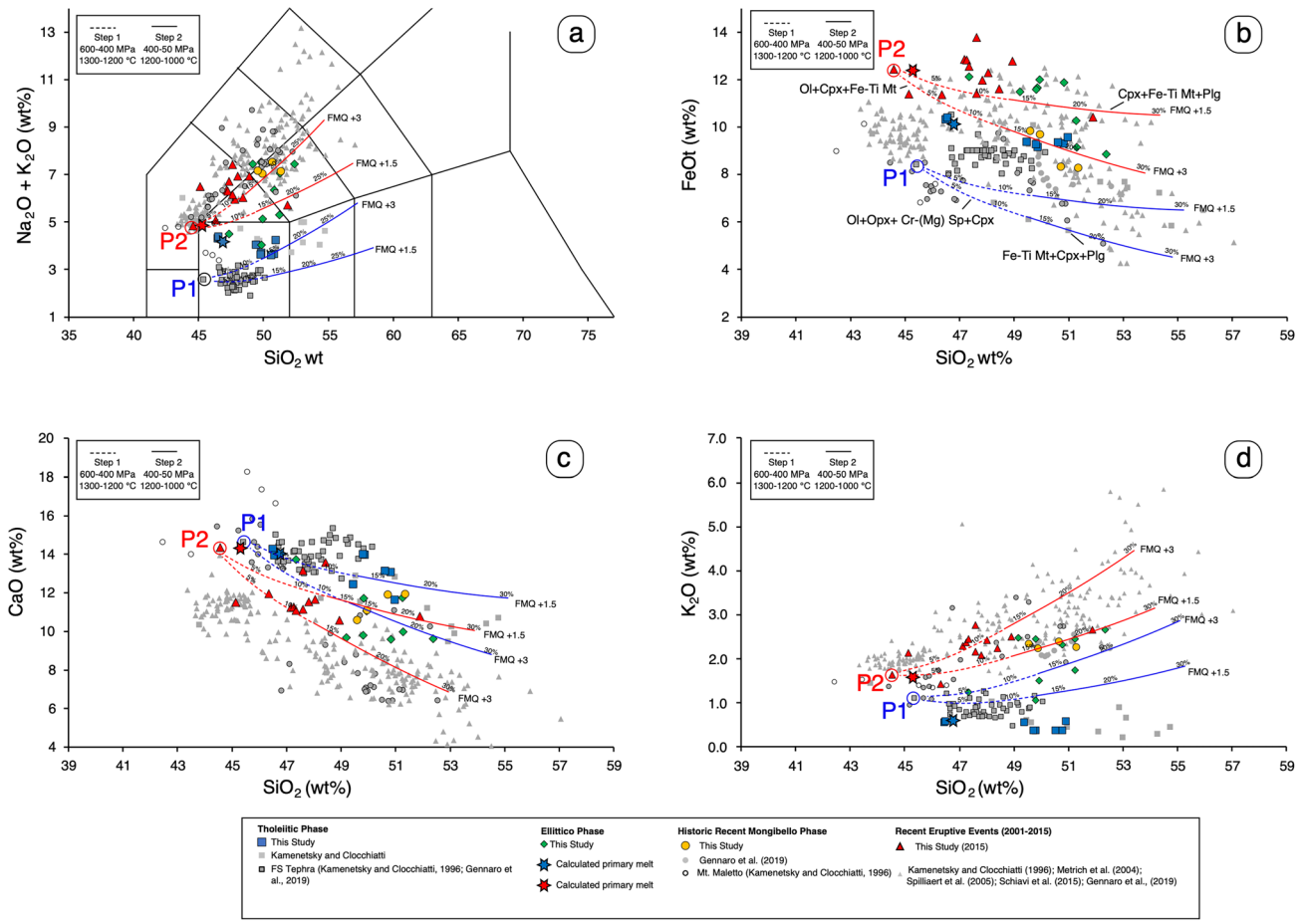


**Fig. 9** Major element composition of studied and bibliographic olivine-hosted MIs. Results in the range of FMQ + 1.5 to + 3 of the rhyolite-MELTS fractionation modelling are plotted as curves starting from the initial subalkaline P1 and alkaline P2 compositions. **a** $SiO_2$ vs $Na_2O + K_2O$; **b** $SiO_2$ vs FeOt; **c** $SiO_2$ vs CaO; **d** $SiO_2$ vs $K_2O$

and Fe-Ti Mt in P2) as well as that of Cpx as a result of the lower $Fe^{2+}/Fe^{3+}$ partitioning in the melt (Pichavant et al. 2002; Feig et al. 2010; Ubide et al. 2019;). It is noteworthy that the liquid line of descent derived from the starting composition P1 closely reproduces a sub-alkaline tholeiitic trend characterized by less pronounced increases in alkali ($Na_2O + K_2O$) and $SiO_2$. These results suggest that the geochemical features of FS Tephra is unsuitable to represent a primordial magma composition of the alkaline series. The products emitted by this eruptive event are the sole example in the etnean suite of sub-alkaline events, erupted during the Recent Mongibello Phase (< 12 ka; Branca et al. 2011).

## Mantle source of volatiles

The undifferentiated nature of the studied MIs allows us to speculate on the composition of the mantle source and on the evolution of the melting processes responsible for the sub-alkaline to alkaline transition (Post-1971, Tanguy et al. 1997; Ferlito et al. 2009; Casetta et al. 2020). Several authors have suggested that Mt. Etna primary magmas are generated by an enriched metasomatized mantle characterized by a mixed peridotitic/pyroxenitic lithologies. Two almost complementary scenarios have been invoked: (i) the increasing contribution of crustal slab-derived components in the mantle source in the last 15Ka (Doglioni et al. 2001; Tonarini et al. 2001; Corsaro and Metrich 2016) or (ii) the multi-stage melting of a veined enriched spinel peridotitic/pyroxenitic mantle characterized by variable eutectic contribution of amphibole and phlogopite (Correale et al. 2014; Casetta et al. 2020).

The main data supporting the first scenario are the high $\delta^{11}B$, and $^{87}Sr/^{86}Sr$ and the low $^{143}Nd/^{144}Nd$, the high Rb/Th in recent 2001 and in FS Tephra (Tonarini et al. 2001; Kamenetsky et al 2007; Schiavi et al. 2015). On the other hand, other studies highlighted the extreme variability in isotopic and Rb/Th ratios, and K content in both pre-historic and recent products suggesting that the temporal increase in subduction-related contribution is weakly supported and more likely resulting by the absence of sufficient data

(Ferlito and Lanzafame 2010; Ferlito et al. 2014). Hence, modal heterogeneities of an enriched mantle characterized by variable amounts of hydrous phases (Amph/Phlog) could also be considered as the main factor constraining the geochemical variability of erupted lavas with time. With this assumption, Casetta et al. (2020) modelled the compositional change from the Tholeiitic Phase to Alkaline and the K-enrichment in recent etnean lavas, invoking two different mantle source domains (named S-1 and S-2), characterized respectively by 2% and 3% modal content of amphibole and 2.5% and 2.7% of phlogopite (Casetta et al. 2020). This result is consistent with the scenario of Beccaluva et al. (1998) and Correale et al. (2018) for the nearby Hyblean magmatism, where two different amphibole + phlogopite-bearing spinel peridotites seems to be required to account for the compositional features of the tholeiitic and alkaline magmas at Mt. Etna.

A slight variation in the Amph/Phlog melting proportions could significantly affect the $H_2O/CO_2$ ratio in primary melt inclusions. In order to verify if this scenario is plausible, a mass balance mantle melting modelling has been performed with the aim to reproduce the observed sub-alkaline and alkaline MIs composition; following the method described by Beccaluva et al. (1998).

Reiterative mass-balance calculations were carried out between two representative MIs compositions (ET4 8/1 Tholeiite and CC2015 109/01 alkaline), selected based on their $SiO_2$, MgO and $CaO/Al_2O_3$, and plausible chemical and mineralogical peridotite source compositions. Calculation was performed by melting (adding) different proportions of the mineral constituting the spinel-lherzolite (Ol, Opx, Cpx and Sp) and re-crystallizing (subtracting) more refractory mineral phases from an harzburgite, both fertile and refractory mineral phases derive from mantle xenoliths embedded in alkaline basalts and basanites from the Hyblean magmatism (Beccaluva et al. 1998). This method allows to take into consideration, the solid-solution constituent which enter the melt, since the most fusible components contribute to the melt formation, especially in the early stage of melting. Resulting sums were normalized to 100% anhydrous and constitute the eutectic proportions of the melting process. The iterative calculation stopped when the $r^2$ (total square residua) was below 1 (Table 3).

The modal content of amphibole and phlogopite in the mantle source and their eutectic contribution during melting should have been significant. Because these mineral phases are generally absent in the Hyblean xenoliths, their composition was taken from the peridotite xenoliths from Kerguelen (Moine et al. 2004).

Starting fertile and refractory mineral phases and the results of the mass-balance calculations are reported in Table 3. The melting process needed to reproduce the tholeiitic MI (ET4 8/1) was characterized by a significant eutectic contribution of amphibole (85%), clinopyroxene (28.8), spinel (3.8%) and orthopyroxene (2%) with a total melting degree of 21.4% and a $r^2 = 0.92$. Conversely, recent alkaline 2015 MIs composition (CC2015 109/01) requires phlogopite in the melting process (12%) together with amphibole (69%) and clinopyroxene (45.3%) and spinel (5.1%) for a total melting degree of 16% and $r^2 = 0.49$. Notably, an increased contribution of clinopyroxene on the eutectic is necessary to reproduce the $SiO_2$-undersaturated composition of alkaline MIs.

Results suggest that modeled MIs compositions could derive from a spinel-lherzolitic source similar to the calculated S2-like source of Beccaluva et al. (1998); constituted by the following assemblage: 54% olivine, 20% orthopyroxene, 15.3% clinopyroxene, 5% spinel, 3% amphibole and 2.7% phlogopite. Variations in the eutectic contributions of Opx/Cpx and Amph/Phlog are the primary aspects constraining the compositions of tholeiitic and alkaline melts. This result is also consistent with those obtained by modelling the trace element composition of reconstructed primary melts from Casetta et al. (2020), where observed Rb/Th, Rb/Nb and Rb/Hf differences between subalkaline and alkaline melts are accounted with slightly changes in the amphibole/phlogopite proportions during partial melting.

The reciprocal stability of amphibole and phlogopite in the mantle, is strongly affected by the composition of the fluxing fluid phase (Green et al. 2014). Considering this complex interplay, the global observed changes in $H_2O/(H_2O + CO_2)$ mol from 0.70 to 0.99 in almost undifferentiated MIs the analyses MI's of this study for in terms of, are apparently not related to the alkaline affinity of Mis. Instead, they could be indirectly related to the composition of primary melts beneath Mt. Etna.

The abundant literature on trace element and isotopic composition of etnean lavas highlighted that the mantle source must be significantly enriched, with prominent HIMU component over a depleted MORB signature (Correale et al. 2014). Most studies agree in considering that the mantle source was strongly metasomatized by alkaline melts/fluids before the onset of the etnean magmatism 550 ka B.P. The effects of $H_2O$ and $CO_2$ in the percolating metasomatic agents are to stabilize amphibole and phlogopite in variable proportions. Hence, the observed change in $H_2O/(H_2O + CO_2)$ mol from 0.94 to 0.92 (Fig. 6) in the less degassed primary MIs could be explained as the result of partial melting of a mantle domain richer in phlogopite and $CO_2$ contributing to increasing the $K_2O$ content in more recent alkaline products.

There is a vivid debate about the role of the Ionian subduction in the genesis of Mt. Etna magmatism. In order to investigate the origin of the volatiles involved in the mantle melting below Etna, a comparison between $H_2O/CO_2$ and Cl/F is shown in Fig. 10. Cl and F are less abundant in

**Table 3** Mantle melting modelling results. Eutectic melting proportions E1 and E2 for the generation of sub–alkaline tholeiite and alkaline melts respectively

| Mantle Mineral Phases | Lherzolite | | | | | | Harzburgite | | |
|---|---|---|---|---|---|---|---|---|---|
| | ol1 | opx1 | cpx1 | sp1 | amph | phlo | ol2 | opx2 | cpx2 |
| $SiO_2$ (wt%) | 40.69 | 55.70 | 53.03 | 0.06 | 42.37 | 40.70 | 39.79 | 55.29 | 51.14 |
| $TiO_2$ (wt%) | 0.00 | 0.15 | 0.51 | 0.71 | 2.50 | 2.74 | 0.00 | 0.06 | 0.49 |
| $Al_2O_3$ (wt%) | 0.00 | 3.25 | 4.43 | 50.21 | 12.10 | 14.30 | 0.00 | 2.95 | 3.45 |
| FeOt (wt%) | 11.36 | 6.98 | 4.21 | 14.77 | 5.69 | 3.65 | 8.84 | 5.46 | 2.90 |
| MgO (wt%) | 48.71 | 32.03 | 17.72 | 19.43 | 16.79 | 23.70 | 50.00 | 33.93 | 16.88 |
| CaO (wt%) | 0.13 | 0.72 | 18.17 | 0.12 | 11.41 | 0.02 | 0.06 | 1.15 | 21.51 |
| Na2O (wt%) | 0.00 | 0.03 | 1.21 | 0.01 | 3.55 | 1.02 | 0.00 | 0.00 | 0.57 |
| K2O (wt%) | 0.00 | 0.00 | 0.00 | 0.01 | 0.72 | 9.09 | 0.00 | 0.00 | 0.00 |
| Total | 100.89 | 98.86 | 99.28 | 85.32 | 95.13 | 95.22 | 98.69 | 98.84 | 96.94 |

| | 8_1 Tholeiite | Norm 100 | Calculated Melt | Error | E1 | % |
|---|---|---|---|---|---|---|
| $SiO_2$ (wt%) | 46.55 | 47.12 | 46.77 | 0.12 | Ol | –20 |
| $TiO_2$ (wt%) | 1.91 | 1.93 | 2.34 | 0.17 | Opx | 2 |
| $Al_2O_3$ (wt%) | 13.6 | 13.77 | 14.20 | 0.19 | Cpx | 29 |
| FeOt (wt%) | 10.38 | 10.51 | 10.12 | 0.15 | Sp | 4 |
| MgO (wt%) | 8.06 | 8.16 | 8.33 | 0.03 | Amph | 85 |
| CaO (wt%) | 13.91 | 14.08 | 14.07 | 0.00 | Phlo | 0 |
| $Na_2O$ (wt%) | 3.83 | 3.88 | 3.55 | 0.10 | Tot | 100 |
| $K_2O$ (wt%) | 0.55 | 0.56 | 0.61 | 0.00 | | |
| Total | 98.79 | 100 | 100 | 0.76 | $r^2$ | 0.87 |
| | 109_1 Alkaline | Norm 100 | Calculated Melt | Error | E2 | % |
| $SiO_2$ (wt%) | 44.57 | 45.22 | 45.36 | 0.02 | Ol | –16 |
| $TiO_2$ (wt%) | 1.94 | 1.97 | 2.31 | 0.12 | Opx | –16 |
| $Al_2O_3$ (wt%) | 14.24 | 14.45 | 14.52 | 0.01 | Cpx | 45 |
| FeOt (wt%) | 12.44 | 12.62 | 12.43 | 0.04 | Sp | 5 |
| MgO (wt%) | 6.21 | 6.30 | 6.15 | 0.02 | Amph | 69 |
| CaO (wt%) | 14.34 | 14.55 | 14.36 | 0.04 | Phlo | 12 |
| $Na_2O$ (wt%) | 3.19 | 3.24 | 3.30 | 0.00 | Tot | 100 |
| $K_2O$ (wt%) | 1.64 | 1.66 | 1.58 | 0.01 | | |
| Total | 98.56 | 100.00 | 100.00 | 0.24 | $r^2$ | 0.49 |

$r^2$, the total square residua

basaltic melts with respect to $H_2O$ and $CO_2$, for this reason they represent only a minor component of the vapor phase (Rowe and Lassiter 2009) despite their lower solubility. Below saturation, Cl and F behave as incompatible elements (similarly to K and Nb). In Fig. 10, Mt. Etna MIs are plotted together with literature data of olivine-hosted MIs from MORB, E-MORB, Ocean Island Basalts and Continental Intraplate Basalts. Since $H_2O$ and Cl-rich fluids tend to be incorporated in oceanic lithosphere during hydrothermalism at oceanic spreading ridges and then released during prograde metamorphism of the subducted slab, arc related magmatism shows a significative higher $H_2O/CO_2$ and Cl/F ratio with respect to MORB and intraplate magmatism. A positive (almost continuous) trend toward higher $H_2O/CO_2$ and Cl/F from MORB to arc volcanism is thus evident in Fig. 10. In this framework Mt. Etna MIs show a significant high Cl/F, partially overlapping the field of arc magmatism. This result, however, does not allow to univocally invoke the active presence of subductive fluids from the current active Ionian slab in Etna mantle source. Recent studies on volatiles in olivine-hosted MIs from alkaline continental rift magmatism demonstrated that fluids from old (> 100 Ma) subduction can be stored in lithospheric and sublithospheric mantle domains and remobilized by subsequent alkaline rift-related magmatism (Rowe and Lassiter 2009; Hudgins et al. 2015; Rowe et al. 2015; Aviado et al. 2015; Stefano et al.

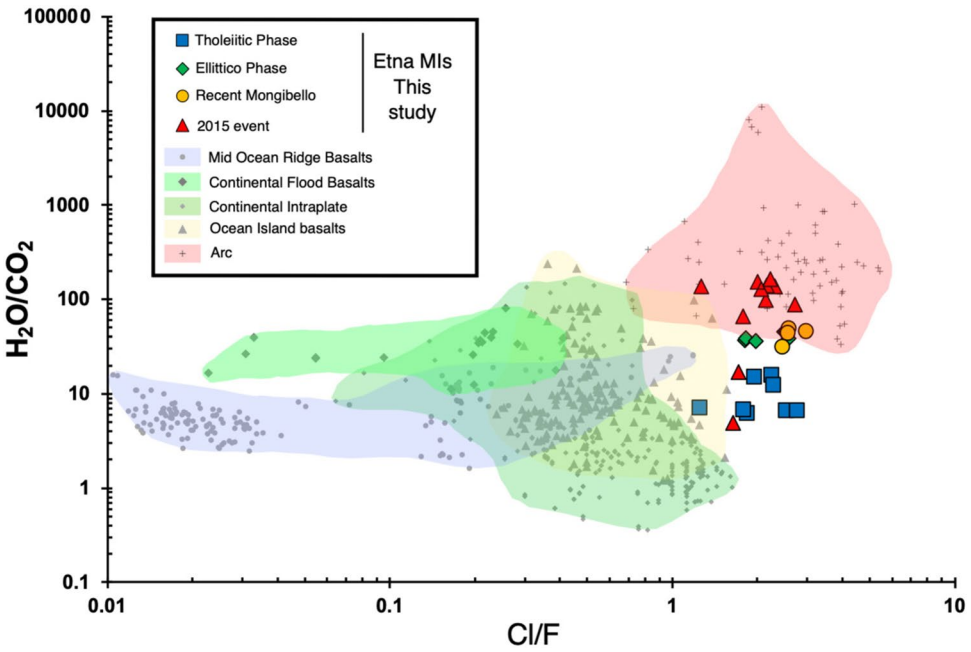


**Fig. 10** $H_2O/CO_2$ versus Cl/F of studied MIs plotted together with bibliographic data from MORB and EMORB (Le Roux et al. 2006; Saal et al. 2002; Shaw et al. 2010; Laubier et al. 2007); intraplate alkaline magmatism (Longprè et al. 2017; Walowsky et al. 2019; Hudgins et al. 2015; Rowe et al. 2015), West Antarctic Rift System (Giacomoni et al. 2020) and arc related basaltic magmas (Cadoux et al. 2018; Rasmussen et al. 2018; Ruscitto et al. 2010; Roggensack et al. 1997; Wade et al. 2006; Portnyagin et al. 2007, 2019; Shaw et al. 2008)

2011; Giacomoni et al. 2020). The alkaline composition of primary magmas and the absence of K, Nb and Ti anomalies in Mt. Etna both subalkaline and alkaline products (Tanguy et al. 1997; Casetta et al. 2020) could be further evidence toward this last scenario.

The occurrence of alkaline anorogenic and volatile-rich magmatism during Plio-Pleistocene on Mt. Iblei and in the Etnean area suggest that this lithospheric domain was significantly metasomatized by alkaline and carbonatitic fluids (Beccaluva et al. 1998). Paleogeographic and geodynamic reconstructions suggest that this domain could have been affected by the dehydration of the S-SE subducting slab of the Alpine Tethys beneath the African continental margin from 120 to 80 Ma (Rosenbaum et al. 2004; Turco et al. 2007; Zarcone and Di Stefano 2010). In this scenario, the lithologies of the Eastern Sicily lithospheric mantle domains were likely affected by metasomatic hydrous fluids/melts enriched in incompatible elements, and this could have resulted in a veined lithospheric mantle in Amph/Phlog. The onset of melting processes of this re-fertilized mantle could have been easily triggered by local lithospheric decompression as a result of the foreland thinning after the Appennine-Maghrebian chain formation (Mt. Iblei magmatism, Beccaluva et al. 1998) or constrained by the left-lateral transtensive movement of the Malta Escarpment (Mt. Etna, Neri et al. 2018). Further trace elements, volatiles and isotopic studies on primary melts are needed to better constrain this hypothesis but this model is consistent with what is observed at the Rio Grande Rift (Rowe and Lassiter 2009; Rowe et al. 2015), the East African Rift (Hudgins et al. 2015) and the West Antarctic Rift (Giacomoni et al. 2020).

## Conclusions

This study confirms the extreme compositional variability of olivine-hosted MIs of Mt. Etna in terms of both major elements and volatiles. Moreover, the HP-HT homogenization procedure allowed to identify a few plausible primary magma compositions for both the subalkaline and alkaline trends of the etnean lavas. Rhyolite-MELTS thermodynamic modelling reproduces the observed liquid lines of descent by fractional crystallization through the magmatic system under variable redox states which, in turn, constrain the appearance of Fe-oxides on the liquidus at the expense of clinopyroxene.

In accordance with previous studies, primary melts on Etna seem significantly enriched in volatile species. Our determinations suggest that undifferentiated basanitic melts could contain up to 6.14 wt% $H_2O$ and 8474 ppm $CO_2$, which lead to up to an initial content of 12,250 ppm $CO_2$ if a constant $H_2O/(H_2O+CO_2)$ mol of 0.92 is assumed.

The Cl/F ratios strongly suggest a contribution from subduction fluids, together with the absence of significant K, Nb and Ta depletions in Etnean primary magma. Mantle melting modelling suggest that a variable eutectic contribution of amphibole and phlogopite in a spinel-lherzolitic mantle source accounts for recognized sub-alkaline and alkaline MIs compositions. We suggest that fluids contained in etnean magmas could have been inherited from the prolonged 120–80 Ma Alpine Tethys subduction and remobilized by melting of Amph/Phlog enriched mantle domains due to lithospheric decompression later on.

**Supplementary Information** The online version contains supplementary material available at https://doi.org/10.1007/s00410-024-02116-1.

**Acknowledgements** We are deeply thankful to Prof. Dustin Trail and Federico Casetta for their technical and manual assistance during the HP-HT homogenization experiments. Finally, we're grateful to Prof. Gordon Moore who edited this manuscript and to Dr. Kyla Iacovino and an anonymous reviewer for their constructive comments.

**Funding** Open access funding provided by Università di Pisa within the CRUI-CARE Agreement. This work was supported by the Italian Minister of Research and Education 5X1000 "Young Researcher Grant" fund to [PPG], provided by the University of Ferrara, by the Italian National Research Program Grants (PRIN) 2017 Project 20178LPCPW to [MC] and by the PRIN2022 project 2022N4FBAA "PROVES: an integrated PetRO-Volcanological monitoring approach applied to Mt. Etna and Stromboli" to [MM] and [PPG].

**Data availability** The dataset generated and analyzed during the current study are available from the corresponding author on reasonable request.



## References

Aiuppa A, Giudice G, Gurrieri S, Liuzzo M, Burton M, Caltabiano T, McGonigle AJS, Salerno G, Shinohara H, Valenza M (2008) Total volatile flux from Mount Etna. Geophys Res Lett. https://doi.org/10.1029/2008gl035871

Allard P, Carbonnelle J, Dajlevic D, Le Bronec J, Morel P, Robe MC, Maurenas JM, Faivre-Pierret R, Martin D, Sabroux JC, Zettwoog P (1991) Eruptive and diffuse emissions of $CO_2$ from Mount Etna. Nature 351:387–391

Andronico D, Scollo S, Cristaldi A, Caruso S (2008) The 2002–2003 Etna explosive activity: tephra dispersal and features of the deposit. J Geophys Res Solid Earth 113:B04209

Aviado KB, Rilling-Hall S, Bryce JG, Mukasa SB (2015) Submarine and subaerial lavas in the West Antarctic rift system: temporal record of shifting magma source components from the lithosphere and asthenosphere. Geochem Geophys Geosystem. https://doi.org/10.1002/2015GC006076

Beccaluva L, Siena F, Coltorti M, Di Grande A, Lo Giudice A, Macciotta G, Tassinari R, Vaccaro C (1998) Nephelinitic to tholeiitic magma generation in a transtensional tectonic setting: an integrated model for the Iblean volcanism, Sicily. J Petrol 39:1547–1576

Bindeman IN, Kamenetsky VS, Palandri J, Vennemann T (2012) Hydrogen and oxygen isotope behaviors during variable degrees of upper mantle melting: example from the basaltic glasses from Macquarie Island. Chem Geol 310–311:126–136

Branca S, Coltelli M, Groppelli G (2011) Geological evolution of a complex basaltic stratovolcano: Mount Etna. Italy Ital J Geosci 130:306–317

Burton M, Sawyer GM (2013) Deep carbon emissions from volcanoes. Rev Mineral Geochem 75:323–354

Buso R, Laporte D, Schiavi F, Cluzel N, Fonquernie C (2022) High-pressure homogenization of olivine-hosted $CO_2$-rich melt inclusions in a piston cylinder: insight into the volatile content of primary mantle melts. Eur J Mineral 34:325–349

Cadoux A, Iacono-Marziano G, Scaillet B, Aiuppa A, Mather TA, Pyle DM, Deloule E, Gennaro E, Paonita A (2018) The role of melt composition on aqueous fluid v.s. silicate melt partitioning of bromine in magmas. Earth Planet Sci Lett 498:450–463

Casetta F, Giacomoni PP, Ferlito C, Bonadiman C, Coltorti M (2020) The evolution of the mantle source beneath Mt. Etna (Sicily, Italy): from the 600 ka tholeiites to the recent trachybasaltic magmas. Int Geol Rev 62(3):338–359

Chen Y, Zhang Y (2008) Olivine dissolution in basaltic melt. Geochim Cosmochim Acta 72:4756–4777

Coltelli M, Del Carlo P, Pompilio M, Vezzoli L (2005) Explosive eruption of a picrite: the 3930 BP subplinian eruption of Etna volcano (Italy). Geophys Res Lett 32:L23307

Correale A, Paonita A, Martello M, Rizzo A, Rotolo SG, Corsaro RA, Di Renzo V (2014) A two-component mantle source feeding Mt. Etna magmatism: insights from the geochemistry of primitive magmas. Lithos 184–187:243–258

Correale A, Martelli M, Paonita A, Scribano V, Arienzo I (2018) A combined study of noble gases, trace elements, and Sr-Nd isotopes for alkaline and tholeiitic lava from the Hyblean Plateau (Italy). Lithos 314–315:59–70

Corsaro RA, Metrich N (2016) Chemical heterogeneity of Mt. Etna magmas in the last 15 ka inferences on their mantle sources. Lithos 252:123–134

Corsaro RA, Pompilio M (2004) Buoyancy-controlled eruption of magmas at Mount Etna. Terra Nova 16:16–22

Dalou C, Mysen BO (2015) The effect of $H_2O$ on F and Cl solubility and solution mechanisms of in aluminosilicate melts at high pressure and high temperature. Am Mineral 100:633–643

Danyushevsky LV, Eggins SM, Fallon TJ (2000) $H_2O$ abundance in depleted to moderately enriched mid-ocean ridge magmas; part I: incompatible behaviour, implications for mantle storage, and origin of regional variations. J Petrol 41:1329–1364

Del Carlo P, Pompilio M (2004) The relationship between volatile content and the eruptive style of basaltic magma: the Etna case. Annals Geophys. https://doi.org/10.4401/ag-4402

Doglioni C, Innocenti F, Mariotti G (2001) Why Mt. Etna? Terra Nova 13:25–31

Feig ST, Koepke J, Snow EJ (2010) Effect of oxygen fugacity and water on phase equilibria of a hydrous tholeiitic basalt. Contrib Mineral Petrol 160:551–568

Ferlito C, Lanzafame G (2010) The role of supercritical fluids in the potassium enrichment of magmas at Mount Etna volcano (Italy). Lithos 119:642–650

Ferlito C, Coltorti M, Cristofolini R, Giacomoni PP (2009) The contemporaneous emission of low-K and high-K trachybasalts and the role of the NE rift during the 2002 eruptive event, Mt. Etna, Italy. Bull Volcanol 71:575–587

Ferlito C, Coltorti M, Lanzafame G, Giacomoni PP (2014) The volatile flushing triggers eruptions at open conduit volcanoes: evidence from Mount Etna volcano (Italy). Lithos 184–187:447–455

Ferrero S, Angel RJ (2018) Micropetrology: are inclusions grains of truth? J Petrol 59:1671–1700

Gennaro E, Iacono-Marziano G, Paonita A, Rotolo SG, Martel C, Rizzo A, Pichavant M, Liotta (2019) Melt inclusions track melt evolution and degassing of Etnean magmas in the last 15 ka. Lithos 324–325:716–732

Gennaro E, Iacono-Marziano G, Paonita A, Moussallam Y, Peters N, Pichavant M, Martel C (2020) Sulphur behavior and oxygen fugacity variation in Mt. Etna system revealed by melt inclusions

Giacomoni PP, Ferlito C, Alesci G, Coltorti M, Monaco C, Viccaro M, Cristofolini R (2012) A common feeding system of the NE and S

rifts as revealed by the bilateral 2002/2003 eruptive event at Mt. Etna (Sicily, Italy). Bull Volcanol 74:2415–2433
Giacomoni PP, Ferlito C, Coltorti M, Bonadiman C, Lanzafame G (2014) Plagioclase as archive of magma ascent dynamics on "open conduit" volcanoes: the 2001–2006 eruptive period at Mount Etna. Earth Sci Rev 138:371–393
Giacomoni PP, Coltorti M, Mollo S, Ferlito C, Braiato M, Scarlato P (2018) The 2011–2012 paroxysmal eruptions at Mt. Etna volcano: insights on the vertically zoned plumbing system. J Volcanol Geotherm Res 349:370–391
Giacomoni PP, Bonadiman C, Casetta F, Faccini B, Ferlito C, Ottolini L, Zanetti A, Coltorti M (2020) Long-term storage of subduction-related volatiles in Northern Victoria Land lithospheric mantle: insight from olivine-hosted melt inclusions from McMurdo basic Lavas (Antarctica). Lithos 378–379:105826
Giacomoni PP, Casetta F, Valenti V, Ferlito C, Lanzafame G, Nazzari M, Coltorti M (2021) Thermo-barometric constraints on the Mt. Etna 2015 eruptive event. Contrib Mineral Petrol 176:88
Green DH, Hibberson WO, Rosenthal A, Kovacs I, Yaxley GM, Falloon TJ, Brink F (2014) Experimental study of the influence of water on melting and phase assemblages in the upper mantle. J Petrol 55:2067–2096
Gualda GAR, Ghiorso MS, Lemons RV, Carley TL (2012) Rhyolite-MELTS: a modified calibration of MELST optimized for silica-rich, fluid-bearing magmatic systems. J Petrol 53:875–890
Hudgins TR, Mukasa SB, Simon AC, Moore G, Barifaijo E (2015) Melt inclusion evidence for $CO_2$-rich melts beneath the western branch of the East African Rift: implications for long-term storage of volatiles in the deep lithospheric mantle. Contrib Mineral Petrol 169:46
Iacono Marziano G, Morizet Y, Le Trong E, Gaillard F (2012) New experimental data and semi empirical parameterization of $H_2O$-$CO_2$ solubility in mafic melts. Geochim Cosmoch Acta 97:1–23
Jochum KP, Stoll B, Herwig K, Willbold M, Hofmann AW, Amini M, Aarburg S, Abouchami W, Hellebrand E, Mocek B, Raczek I, Stracke A, Alard O, Bouman C, Becker S, Ducking M, Bratz H, Klemd R, de Bruin D, Canil D, Cornell D, de Hoog CJ, Dalpe C, Danyushevsky L, Eisenhauer A, Gao YJ, Snow JE, Goschopf N, Gunther D, Latkoczy C, Guillong M, Hauri EH, Hofer HE, Lahaye Y, Horz K, Jacob DE, Kassemann SA, Kent AJR, Ludwig T, Zack T, Mason PRD, Meixner A, Rosner M, Misawa KJ, Nash BP, Pfander J, Premo WR, Sun WD, Tiepolo M, Vannucci R, Vennemann T, Wayne D, Woodhead JD (2006) MPI-DING reference glasses for in situ microanalysis: new reference values for element concentrations and isotope ratios. Geochem Geoph Geosyst. https://doi.org/10.1029/2005GC001060
Kamenetsky V, Clocchiatti R (1996) Primitive magmatism of Mt. Etna: insights from mineralogy and melt inclusions. Earth Planet Sci Lett 142:553–572
Kamenetsky VS, Pompilio M, Metrich N, Sobolev AV, Kuzmin DV, Thomas R (2007) Arrival of extremely volatile-rich high-Mg magmas changes explosivity of Mount Etna. Geology 35:255–258
Keppler H, Wiedenbeck M, Shcheka SS (2003) Carbon solubility in olivine and the mode of carbon storage in the Earth's mantle. Nature 424:414–416
Lachance GR, Trail RJ (1966) Practical solution to the matrix problem in X-ray analysis. Can Spectrosc 11:43–48
Laubier M, Schiano P, Doucelance R, Ottolini L, Laporte D (2007) Olivine-hosted melt inclusions and melting processes beneath the FAMOUS zone (Mid-Atlantic Ridge). Chem Geol 240:129–150
Le Bas MJ, Le Maitre RW, Streckeisen A, Zanettin B (1986) A chemical classification of volcanic rocks based on the total alkali-silica diagram. J Petrol 27:745–750
Le Roux PJ, Shirey SB, Hauri EH, Perfit MR, Bender JF (2006) The effects of variable sources, processes and contaminants on the composition of northern EPR MORB (8–10°N and 12–14°N): evidence from volatiles ($H_2O$, $CO_2$, S) and halogens (F, Cl). Earth Planet Sci Lett 251:209–231
Longpré MA, Stix J, Klugel A, Shimizu N (2017) Mantle to surface degassing of carbon and sulphur-rich alkaline magma at el El Hierro, Canary Islands. Earth Planet Sci Lett 460:268–280
Metrich N, Clocchiatti R (1989) Melt inclusion investigation of the volatile behaviour in historic alkali basaltic magmas of Etna. Bull Volcanol 51:185–198
Metrich N, Allard P, Spilliaert N, Andronico D, Burton M (2004) 2001 flank eruption of the alkali- and volatile-rich primitive basalt responsible for Mount Etna's evolution in the last three decades. Earth Planet Sci Lett 228:1–17
Moine BN, Grégoire M, O'Reilly SY, Delpech G, Sheppard SMF, Lorand JP, Renac C, Giret A, Cottin JY (2004) Carbonatite melt in oceanic upper mantle beneath the Kerguelen Archipelago. Lithos 75:239–252
Mollo S, Giacomoni PP, Coltorti M, Ferlito C, Iezzi G, Scarlato P (2015) Reconstruction of magmatic variables governing recent Etnean eruptions: constraints from mineral chemistry and P-T-$fO_2$-$H_2O$ modelling. Lithos 212–215:311–320
Neri M, Rivalta E, Maccaferri F, Acocella V, Cirrincione R (2018) Etnean and Hyblean volcanism shifted away from the Malta Escarpment by crustal stresses. Earth Planet Sci Lett 486:15–22
Newman S, Lowenstern JB (2002) VolatileCalc: a silicate melt-$H_2O$-$CO_2$ solution model written in Visual Basic for excel. Comput Geosci 28:597–604
Pichavant M, Martel C, Bourdier JL, Scaillet B (2002) Physical conditions, structure, and dynamics of a zoned magma chamber: mount Pele e (Martinique, Lesser Antilles Arc). J Geoph Res. https://doi.org/10.1029/2001JB000315
Portnyagin M, Hoernle K, Plechov P, Mironov N, Khbunaya S (2007) Constraints on mantle melting and composition and nature of slab components in volcanic arcs from volatiles ($H_2O$, S, Cl, F) and trace elements in melt inclusions from the Kamchatka Arc. Earth Planet Sci Lett 225:53–69
Portnyagin M, Mironov N, Gurenko A, Almeev RR, Luft C, Holtz F (2019) Dehydration of melt inclusions in olivine and implications for the origin of silica-undersaturated island-arc melts. Earth Planet Sci Lett 517:95–105
Putirka K, Perfit M, Ryerson FJ, Jackson MG (2007) Ambient and excess mantle temperatures, olivine thermometry, and active vs. passive upwelling. Chem Geol 241:177–206
Rasmussen DJ, Plank TA, Roman DC, Powerm JA (2018) When does eruption run-up begin? Multidisciplinary insight from the 1999 eruption of Shishaldin volcano. Earth Planet Sci Lett 408:1–14
Rasmussen DJ, Plank TA, Wallace PJ, Newcombe ME, Lowenstern JB (2020) Vapor bubble growth in olivine-hosted melt inclusions. Am Mineral 106(12):1898–1919. https://doi.org/10.2138/am-2020-7377
Roeder PL, Emslie RF (1970) Olivine-liquid equilibrium. Contrib Mineral Petrol 29:275–289
Roggensack K, Hervig RL, McKnight SB, Williams SN (1997) Explosive basaltic volcanism from Cerro Negro Volcano: influence of volatiles on eruptive style. Science 277:1639–1642
Rosenbaum G, Lister G, Duboz C (2004) The Mesozoic and Cenozoic motion of Adria (central Mediterranean): a review of constraints and limitations. Geodin Acta 17:125–139
Rowe MC, Lassiter JC (2009) Chlorine enrichment in central Rio Grande Rift basaltic melt inclusions: evidence for subduction modification of the lithospheric mantle. Geology 37:439–442
Rowe MC, Lassiter JC, Goff K (2015) Basalt volatile fluctuations during the continental rifting: an example from the Rio Grande Rift

USA. Geochem Geophys Geosyst. https://doi.org/10.1002/2014GC005648

Ruscitto DM, Wallace PJ, Johnson ER, Kent AJR, Binderman IN (2010) Volatile contents of mafic magmas from cinder cones in the Central Oregon High Cascades: implications for magma formation and mantle conditions in a hot arc. Earth Planet Sci Lett 298:153–161

Saal AE, Hauri EH, Langmuir CH, Perfit MR (2002) Vapor undersaturation in primitive mid-ocean-ridge basalt and the volatile content of Earth's upper mantle. Nature 419:451–455

Schiano P, Crocchiati R, Ottolini L, Bus T (2001) Transition of Mount Etna lavas from a mantle-plume to an island-arc magmatic source. Nature 412:900–904

Schiavi F, Rosciglione A, Kitagawa H, Kobayashi K, Nakamura E, Mario Nuccio P, Ottolini L, Paonita A, Vannucci R (2015) Geochemical heterogeneities in magma beneath Mount Etna recorded by 2001–2006 melt inclusions. Geochem Geophys Geosyst. https://doi.org/10.1002/2015GC005786

Schiavi F, Provost A, Schiano P, Cluzel N (2016) P-V–T–X evolution of olivine-hosted melt inclusions during high-temperature homogenization treatment. Geochim Cosmochim Ac 172:1–21

Shaw AM, Hauri EH, Fischer TP, Hilton DR, Kelley KA (2008) Hydrogen isotopes in Mariana arc melt inclusions: implications for subduction dehydration and the deep- Earth water cycle. Earth Planet Sci Lett 275:138–145

Shaw A, Behn MD, Humphries SE, Sohn RA, Gregg PM (2010) Deep pooling of low degree melts and volatile fluxes at the 85 E segment of the Gakkel Ridge: evidence from olivine-hosted melt inclusions and glasses. Earth Planet Sci Lett 289:311–322

Shcheka SS, Wiedenbeck M, Frost DJ, Keppler H (2006) Carbon solubility in mantle minerals. Earth Planet Sci Lett 245:730–742

Shishkina TA, Botcharnikov RE, Holtz F, Almeev RR, Portnyagin MV (2010) Solubility of $H_2O$- and $CO_2$- bearing fluids in tholeiitic basalts at pressure up to 500 MPa. Chem Geol 277:115–125

Spilliaert N, Allard P, Metrich N, Sobolev AV (2006a) Melt inclusion record of the conditions of ascent, degassing, and extrusion of volatile-rich alkali basalt during the powerful 2002 flank eruption of Mount Etna (Italy). J Geophys Res Solid Earth 111:B04203. https://doi.org/10.1029/2005JB003934

Spilliaert N, Metrich N, Allard P (2006b) S-Cl-F degassing pattern of water-rich alkali basalt: modelling and relationship with eruption styles on Mount Etna volcano. Earth Planet Sci Lett 248:772–786

Stefano CJ, Mukasa SB, Andronikov A, Leeman WP (2011) Water and other volatile systematics of olivine-hosted melt inclusions from the Yellowstone hotspot track. Contrib Mineral Petrol 161:615–633

Tanguy J-C, Condomines M, Kieffer G (1997) Evolution of the Mount Etna magma: constraints on the present feeding system and eruptive mechanism. J Volcanol Geotherm Res 75:221–250

Tingle TN, Green HW, Finnerty AA (1988) Experimental and observations bearing on the solubility and diffusivity of carbon in olivine. J Geoph Res Solid Earth 93:289–315

Tonarini S, Armienti P, D'Orazio M, Innocenti F (2001) Subduction-like fluids in the genesis of the Mt. Etna magmas: evidence from boron isotopes and fluid mobile elements. Earth Planet Sci Lett 5989:1–13

Toplis MJ (2005) The thermodynamics of iron and magnesium partitioning between olivine and liquid: criteria for assessing and predicting equilibrium in natural and experimental systems. Contrib Mineral Petrol 149:22–39

Turco E, Schettino A, Nicosia U, Santantonio M, Di Stefano P, Iannace A, Cannata D, Conti MA, Deiana G, D'Orazi Porchetti S, Felici F, Liotta D, Mariotti M, Milia A, Petti FM, Pierantoni PP, Sacchi E, Sbrescia V, Tommasetti K, Valentini M, Zamparelli V, Zarcone G (2007) Mesozoic Paleogeography of the Central Mediterranean Region. Geoitalia, VI Forum Italiano di Scienze della Terra. Epitome, 2: 108

Ubide T, Caulfield J, Brandt C, Bussweiler Y, Mollo S, Di Stefano F, Nazzari M, Scarlato P (2019) Deep magma storage revealed by multi-method elemental mapping of clinopyroxene megacrysts at Stromboli volcano. Front Earth Sci. https://doi.org/10.3389/feart.2019.00239

Wade JA, Plank T, Melson WG, Soto GJ, Hauri EH (2006) Volatile content of magmas from Arenal volcano, Costa Rica. J Volcanol Geotherm Res 157:94–120

Wallace PJ, Plank T, Bodnar RJ, Gaetani GA, Shea T (2021) Olivine-hosted melt inclusions: a microscopic perspective on a complex magmatic world. Annu Rev Earth Planet Sci 49:465–494

Walowsky KJ, Kirsten LA, De Hoog JCM, Elliott TR, Savov IP, Jones RE (2019) Investigating ocean island mantle source heterogeneity with boron isotopes in melt inclusions. Earth Planet Sci Lett 508:97–108

Watson EB, Wark DA, Price JD, Van Orman JA (2002) Mapping the thermal structure of solid media pressure assemblies. Contrib Mineral Petrol 70:119–134

Zarcone G, Di Stefano P (2010) La Piattaforma Carbonatica Panormide: un caso anomalo nell'evoluzione dei bacini della Tetide giurassica. Ital J Geosci (boll Soc Geol It) 129:188–194

Zhang YX, Stolper EM (1991) Water diffusion in a Basaltic Melt. Nature 351:306–309